UC Irvine
UC Irvine Electronic Theses and Dissertations

Title

Design and Fabrication of Fused Silica Dual-Shell Resonators for High Frequency Symmetry and High Quality Factor

Permalink

https://escholarship.org/uc/item/48v519q2

Author

Meira Lopez, Lois

Publication Date

2025

Peer reviewed|Thesis/dissertation

eScholarship.org Powered by the California Digital Library
University of California

UNIVERSITY OF CALIFORNIA,
IRVINE

Design and Fabrication of Fused Silica Dual-Shell Resonators for High Frequency Symmetry and High Quality Factor

THESIS

submitted in partial satisfaction of the requirements
for the degree of

MASTER OF SCIENCE

in Mechanical and Aerospace Engineering

by

Lois Meira López

Thesis Committee:
Andrei M. Shkel, Chair
Camilo Velez Cuervo
J. Michael McCarthy

2025

© 2025 Lois Meira López

TABLE OF CONTENTS

Page

LIST OF FIGURES **iv**

LIST OF TABLES **vi**

ACKNOWLEDGMENTS **vii**

ABSTRACT OF THE THESIS **viii**

1 Introduction **1**

2 Background **4**
2.1 The Coriolis Vibratory Gyroscope 5
2.2 Performance Parameters of a CVG 7
2.3 Energy Loss Mechanisms in MEM Resonators 10
2.4 The Dual-Shell Resonator Gyroscope (DSG) 13

3 Low-Stress Topology Design for High Quality Factor **17**
3.1 Quality Factor 17
3.2 Energy Loss Mechanisms 19
3.3 Design for Low Anchor Loss 21
3.4 Anchor Loss Simulation 22
3.5 Simulation results 24
3.6 Fabrication of resonators 26
3.7 Characterization of devices 27
3.8 Conclusions 29

4 Identification of Structural Imperfections **30**
4.1 Frequency Symmetry 31
4.2 Method 32
4.3 Simulation and Experimental Results 37
4.4 Conclusions 38

5 Future Work **40**
5.1 Radial deviations 40
5.2 Junction tilt 42
5.3 Stem shift 44

5.4 Suggested improvements to fabrication 44

6 Conclusions **46**

Bibliography **48**

Appendix A List of Vendors **54**

LIST OF FIGURES

Page

2.1 Schematic of a MEMS coriolis vibratory gyroscope as a two (x,y) degree-of-freedom (DOF) mass-spinrg-damper system. The measured rotation Ω_{Sensed} is around the direction perpendicular to the XY plane. 5
2.2 Response of a CVG operated in (a) rate mode; open-loop mode, (b) rate mode; closed-loop mode (force-to-rebalance), and (c) whole-angle mode. . . . 6
2.3 A schematic illustration of an Allan Deviation plot in log-log scale [1]. 9
2.4 A schematic illustration of an PSD plot in log-log scale [2]. 10
2.5 Photograph of Fused Silica Dual-Shell resonator. a) Stem and outer shell serve as a double-ended anchor, b) The junction (blue) is where the outer shell and stem connect to the inner shell (red). 13
2.6 a) The first five vibrational modes of a typical Dual-Shell Resonator. b) Respective mode shape of out-of-plane displacement. The n=2 wineglass mode is preferable due to a higher angular gain in whole-angle operation. 14
2.7 Fabrication process for Dual-Shell resonators [3]. 15

3.1 Schematic of how Dual-Shell Geometry is predicted during design process. a) Dimensions of the donut cavities etched into glass during the wet etching step. b) During glassblowing simulation, the depth, size and relative position between the cavities generate a unique Dual-Shell geometry. c) Grinding and polishing remove material and only the final resonator is left behind. 21
3.2 A family of topologies were considered, where inner-shell geometry (red) changes from hemispherical (rightmost) to hemitoroidal (leftmost). 22
3.3 Simulation of anchor losses. a) A spherical Perfectly Matched Layer (PML) absorbs acoustic waves and is used to estimate energy lost from the resonator through attachment. b) Mesh convergence plot. ∼1.5 million DOF (right) was used for all simulations. 24
3.4 a) FEA results for Q_{Anchor} for different topologies. Hemitoroidal shells (Designs #1-3) are found to have higher Q_{Anchor} limit than hemispherical shells (Designs #7-9). b) Close-up results for n=3 mode, where a maximum is found for Design #4. 25
3.5 Modal stress tensor components as a function of design topology. Modal stresses are automatically normalized by FEA software. Identical trends were found for out-of-plane stress (this figure, solid lines) and Q_{Anchor} (Fig. 4) in both n=2 and n=3 modes. 25

3.6 a) Schematic of experimental setup showing Dual-Shell resonator inside vacuum chamber for characterization. b) Picture of setup in laboratory during Dual-Shell characterization. 27
3.7 Experimental quality factor (maximum of the two degenerate modes) in n=2 (left, red) and n=3 (right, blue). Dashed lines were manually fitted to showcase trends from Figure 3.4. Resonators are ordered from low frequency mismatch (left) to high (right) within each design. 29

4.1 Three types of asymmetries considered in this study. 32
4.2 Rim deviation function fitted to measurements for subsequent importing to FEM model. All five devices exhibit similar deviations in varying magnitudes. Device #1 is shown for illustration purpose. 33
4.3 a) Bottom view (Fig. 4.1) of the rim of DSG resonator. Images are manually stitched into position using overlapping features. b) Side-view of the resonator, where tilt of the junction can be observed and measured. 35
4.4 Identified rim imperfections in device #1 transferred to a solid model: the asymmetric COMSOL mesh was used for subsequent frequency analysis. The legend illustrates deviation from an idealized, perfectly symmetric DSG structure. 35
4.5 Measured and simulated frequency mismatch for n=2 and n=3 wineglass modes. The method was applied to a wide range of frequency mismatches. . 36
4.6 Decomposition of the simulated frequency splits into the different asymmetry types for n=2. For n=3, it was found that the only contributing asymmetry was the deviations of the rim shape from circular. 36
4.7 Harmonic content of the functions fitted to radius deviations. Only the 4th and 6th harmonics contribute to frequency split for n=2 and n=3, respectively, and are highlighted by red and blue regions on the plot. 38

5.1 a) Left: temperature gradient used as an input to the 3D Glassblowing simulation. Right: resulting geometry of a Dual-Shell highlighting the exaggerated junction tilt. b) Left/Right: SEM images of defects in the glass caused by deficient masking during hydrofluoric acid etching. Center: schematic view of a typical etched donut cavity for Dual-Shell fabrication. 41
5.2 a) Polarization sensitive microscope picture, where bonded areas appear solid in color (green outline) and not bonded areas are detected as color gradients (red outline). b) Geometry setup of the cavity for the FEM 3D glassblowing simulation. c) Simulation showing tilting of the inner shell as a result (cyan). 43

LIST OF TABLES

Page

3.1 Geometric parameters and their values that were kept constant in all considered topologies. 22

ACKNOWLEDGMENTS

I would like to thank my parents Pablo and Eva, my brother Xoán, and the rest of my family, for their unconditional support.

I am also deeply grateful for my friends here in Irvine, who are my family away from home.

I am thankful for the guidance of my PI, Professor Shkel, who provided me with the opportunity to join the Microsystems Lab and has been a great source of inspiration. I would also like to thank my colleagues and mentors Chico, Austin, Eudald, and particularly Dani, who taught me everything I needed when I first joined.

Special thanks to the INRF Cleanroom staff, Richard, CY and Mo, as well as Esther, May, Titus, and Matthew, who helped with the fabrication efforts.

This work wouldn't be possible without the financial support of the Balsells Fellowship, which kick-started my studies at UC Irvine and for which I am specially thankful, as well as the Paul and Beverly Holmes Endowed Fellowship.

Finally, I would like to thank the funding support from Integrated Photonics For Sustained Operations, Collaboration Agreement 2022137-142232, under which much of this work was performed.

ABSTRACT OF THE THESIS

Design and Fabrication of Fused Silica Dual-Shell Resonators for High Frequency Symmetry and High Quality Factor

By

Lois Meira López

Master of Science in Mechanical and Aerospace Engineering

University of California, Irvine, 2025

Andrei M. Shkel, Chair

High performance and low SWaPC MEMS gyroscopes are needed for improving and enabling new inertial positioning and navigation applications. The Fused Silica (FS) Dual-Shell μ-HRG (DSG) is a novel implementation of the hemispherical resonator concept. It has a potential for high quality factors thanks to its fundamentally low TED Q limit of ∼60 Million, and the glassblowing on the micro-scale fabrication process can produce shell geometries with low as-fabricated frequency mismatch thanks to surface tension driven fabrication process. However, consistent high quality factors and frequency symmetry are complex to achieve in practice. In this thesis, each of these two fundamental metrics have been studied in detail to overcome current challenges in the resonator's design and fabrication. The contributions of this thesis are:

- Studied the effect of topology on anchor losses of the Dual-Shell resonator and fabricated optimized devices that consistently achieved quality factors above 3 Million, and up to 3.9 Million, more than a 50 % compared to previous results. The relevance of out-of-plane stresses in complex 3D resonators has been understood, and this approach demonstrated the importance of minimizing modal stresses at the anchor to achieve high quality factors.

- Presented a optical image processing method for identifying the imperfections in geometry causing large and small frequency mismatch in Dual-Shell resonators. Frequency mismatches of five devices -varying from 100 to 1000 Hz- were accurately predicted. The modeling approach allowed to observe separately the effect of three different types of imperfections, as well as how they can impact the degeneracy of n=2 and n=3 modes differently.

- The three main types of imperfections were studied from a fabrication point of view, linking them to non-idealities introduced during the fabrication process. This serves as a basis for the suggestion of process improvements and changes that could improve resonator symmetry in future devices.

Chapter 1

Introduction

In today's world, Micro-Electro-Mechanical Systems (MEMS) inertial sensors are widely used for smartphones, automobiles, and consumer electronics in general [4]. However, there is a need for higher-end performance in order to improve existing applications and enable new ones, such as autonomous driving, mixed reality, self-contained navigation, industrial autonomous robots, and micro-satellites. Traditional MEMS inertial sensors are almost exclusively silicon-based and are fabricated by using widely-available micro-machining technologies in the current semiconductor manufacturing industry. However, silicon MEMS technology fundamentally suffers from non-optimal material properties and large fabrication imperfections. New better-suited materials and associated fabrication techniques are needed to push the performance of next-generation MEMS inertial sensors and applications.

Silicon dioxide, most commonly known as glass, is a highly promising material thanks to its excellent mechanical, chemical, and thermal properties. Its mechanical strength is comparable to silicon, but it is more chemically inert and features lower coefficient of thermal expansion (CTE) and thermal conductivity. These thermal properties are key to lowering losses due to thermoelastic damping (TED) in resonators [5]. In addition, its amorphous

nature makes for an isotropic material that won't suffer asymmetries from misalignment between the crystal structure and geometry of the resonator. Currently, only a few processes exist to batch-fabricate MEMS with glass. Among them, glassblowing on the micro-scale is an innovative process that allows for the batch-fabrication of 3D glass shell structures [6; 7]. A hemispherical shell is the core sensing element of a Hemispherical Resonator Gyroscope (HRG). Using micro-scale glassblowing process, the feasibility of fabricating hemispherical shell resonators with sub-Hz frequency symmetry [8] and high quality factors [9] has been demonstrated.

Macro-scale HRGs have achieved great success due to their high sensitivity, extremely low dissipation, environmental stability, and robust operation in high-end defense and space applications [10]. However, their cost and size, mainly driven by their machining-based method of fabrication, heavily limit their applications. The Dual-Shell micro-scale HRG (DSG) is a novel implementation of the hemispherical resonator concept [3], showing potential for ease of integration, frequency symmetry, and extremely high quality factor on the micro-scale, as well as the inherited properties from classical HRGs of continuous operation despite mechanical shock, vibrations, radiation, and harsh thermal conditions. Previous work on the development of Dual-Shell resonators has demonstrated frequency symmetry in the order of a few Hz and quality factors of up to 1.2 million for n=2 wineglass mode of vibration [11], as-fabricated and in a few devices. In addition, a previous study suggested that geometry of the Dual-shell can play a critical role in anchor losses [12]. It is within this context that this research strives to understand the nature of energy losses and frequency asymmetry, and optimize the Dual-Shell design and fabrication so as to consistently achieve high frequency symmetry and high quality factor for most of the devices in each fabricated wafer.

This thesis has the following structure:

- Chapter 2: The physics and operational principle of a Coriolis Vibratory Gyroscope

(CVG) are introduced. An equivalent 2 Degree-of-Freedom (DOF) Mass-Spring-Damper system is proposed to model the dynamics of the hemispherical resonator. Its ruling equations are presented, and key operational and performance parameters are introduced and studied. The contributions to energy losses in MEMS resonators are analyzed. Finally, the fabrication process of an environmentally robust and micro-scale batch fabrication-compatible HRG, the Dual-Shell Resonator Gyroscope, is presented.

- Chapter 3: The energy dissipation mechanisms are independently evaluated and reduced to one critical unresolved source of energy loss: mechanical waves transmitted to the substrate through the anchor of the resonator. This phenomena is exposed as the intrinsically generated stress on the support point due to reaction forces of the wineglass mode of vibration. A design-space study was performed using Finite Element Method (FEM) software. Optimal designs were found, fabricated, and demonstrated experimentally.

- Chapter 4: The problem of frequency symmetry for hemispherical resonators is presented. A non-contact metrology technique for asymmetry identification is introduced. This technique allowed to identify three key types of geometrical features that introduce degeneracy, as well as their relative contribution.

- Chapter 5: The deviations from ideal geometry that were found in the previous chapter are linked to non-idealities in the fabrication process, and mitigation techniques are suggested to increase the overall symmetry of devices.

In conclusion, this thesis presents a thorough study of the fundamental limits to mechanical performance of Dual-Shell hemispherical resonator gyroscope. The aim is to achieve consistently high quality factor and low frequency mismatch, and the subsequent chapters go into the analysis and modeling of the resonator element and its fabrication process to this end.

Chapter 2

Background

We start with reviewing the principle of operation of a CVG and its key performance parameters. Common terms used throughout the thesis are also introduced, and the implementation and fabrication process of a type of CVG, the HRG, is presented.

2.1 The Coriolis Vibratory Gyroscope

The core of the CVG is an oscillating mass with two degenerate modes of vibration. A Coriolis force proportional to an external rotation leads to a transfer of energy between the modes [13]. Thus, tracking the vibration of the modes can be used to sense rotations.

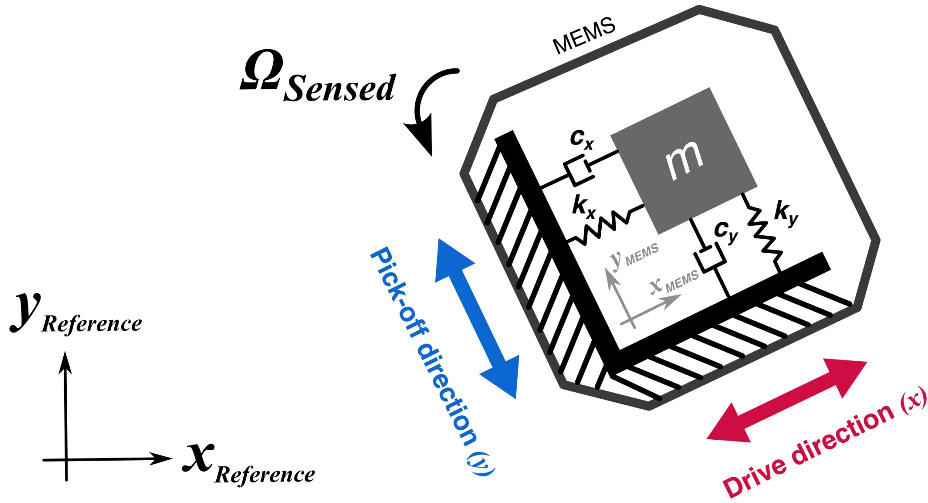

Figure 2.1: Schematic of a MEMS coriolis vibratory gyroscope as a two (x,y) degree-of-freedom (DOF) mass-spinrg-damper system. The measured rotation Ω_{Sensed} is around the direction perpendicular to the XY plane.

The degenerate modes resonator can be modeled as a two degree-of-freedom (DOF) lumped mass-spring-damper system, for which the equations of motion in matrix form can be written as:

$$\begin{bmatrix} \ddot{x} \\ \ddot{y} \end{bmatrix} + \begin{bmatrix} 2\xi_0\omega_0 & 0 \\ 0 & 2\xi_0\omega_0 \end{bmatrix} \begin{bmatrix} \dot{x} \\ \dot{y} \end{bmatrix} + \begin{bmatrix} \omega_0^2 & 0 \\ 0 & \omega_0^2 \end{bmatrix} \begin{bmatrix} x \\ y \end{bmatrix} = \begin{bmatrix} F_x/m \\ F_y/m \end{bmatrix} + \begin{bmatrix} 2\Omega\dot{y} \\ -2\Omega\dot{x} \end{bmatrix}, \tag{2.1}$$

where ω_0 is the resonant frequency when the resonator is mode-matched, Ω is the input

angular rate, ξ_0 is the damping ratio, and m is the effective mass of the system. F_x, and F_y are the control forces along each axis of the resonator. The X axis is typically referred to as *drive* and the Y axis as *sense*.

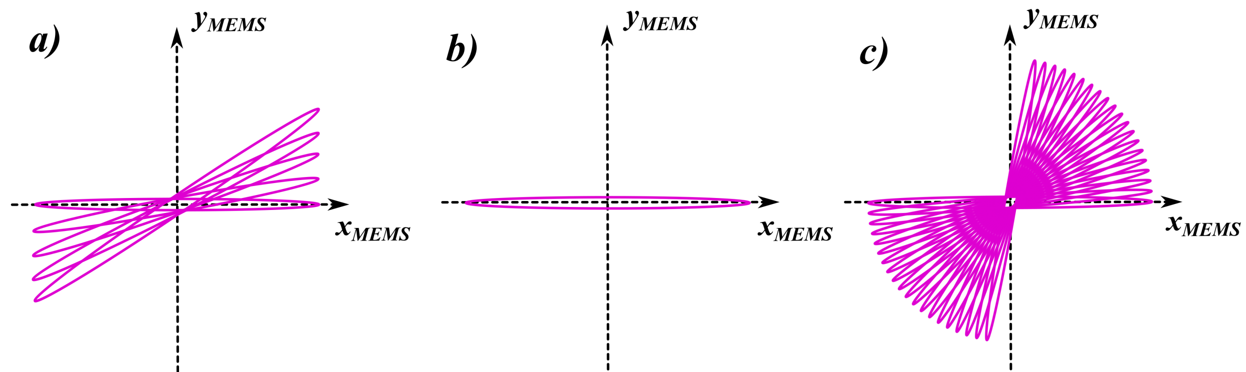

Figure 2.2: Response of a CVG operated in (a) rate mode; open-loop mode, (b) rate mode; closed-loop mode (force-to-rebalance), and (c) whole-angle mode.

CVGs can be classified into two categories depending on how they are operated: rate gyroscopes, that measure angular velocity, and whole-angle gyroscopes (also known as rate-integrating), which measure angle of rotation.

- In the rate mode of operation, an oscillation of a set amplitude is established along the drive axis. When an out-of-plane rotation occurs, Coriolis acceleration coupling generates an oscillation along the sense axis. The amplitude of this oscillation in the sense axis is linearly related to the angular velocity of the external rotation. At this point, two detection schemes can be implemented: open-loop (Figure 2.2a), where the magnitude of the oscillations of the sense axis is measured, or closed-loop (Figure 2.2b), where a control force is applied on the sense axis to stop it from oscillating. Rotation rate is then inferred from the amount of force needed to keep the sense axis from oscillating. This last method is also known as force-to-rebalance (FRB).
- In the whole-angle mode of operation (Figure 2.2c), the resonating mass freely oscillates and the orientation of vibration precesses proportionally to the external vibration. As

a result, tracking the orientation of the vibration yields the angle and has theoretically unlimited mechanical bandwidth.

2.2 Performance Parameters of a CVG

To achieve the highest performing gyroscope, the critical properties and design parameters of a CVG must be identified to maximize sensitivity and minimize the sources of noise.

- The **Angular Gain** A_g is the mechanical sensitivity to the Coriolis force. It is determined by the mass distribution of the sensing element. In the whole-angle mode of operation, the precession angle of the oscillation pattern, θ, can be expressed as [14]:

$$\theta = \theta_0 - A_g \int_{t_0}^{t} \Omega(\tau)\, d\tau \tag{2.2}$$

which is the integral form of

$$\dot{\theta} = -A_g \Omega, \tag{2.3}$$

where $\dot{\theta}$ is the rate of precession and Ω the angular velocity of an external rotation.

- **Mechanical Scale Factor** is the ratio between the sense axis displacement Y and an external angular velocity Ω, and must be maximized for the highest sensitivity. If the resonator has an imperfect geometry (asymmetries), the mechanical scale factor is [15]:

$$SF_{\text{mech}} = \frac{Y}{\Omega} = \frac{2A_g X \omega_x}{\sqrt{(\omega_y^2 - \omega_x^2)^2 + \left(\frac{\omega_x \omega_y}{Q_y}\right)^2}}, \tag{2.4}$$

where X is the vibration amplitude along the drive mode, Q_y is the quality factor (Q-factor) of the sense mode, and ω_x and ω_y are the resonance frequency along the drive and sense axis respectively. It is desirable to achieve perfectly symmetric resonators, leading to mode-matching $\omega_x = \omega_y = \omega_0$ which maximizes SF for a each device, as seen in equation 2.4.

- **Angle Random Walk (ARW)** is white noise caused by mechanical-thermal noise (MTN) and thermo-electrical noise and defines the random walk of angle estimation during navigation. It shows as a slope of 0.5 in a log-log scale Allan Deviation plot (Figure 2.3). Meanwhile, ARW is characterized by the flat part (slope 0) in log-log plot of Power Spectral Density (PSD) which provides information of the signal in the frequency domain (Figure 2.4). ARW caused by MTN is typically the theoretical limit of the noise performance of a rate gyroscope, which can be approximate as the MTN equivalent rate in the form of [16]:

$$\Omega_{ARW} \approx \sqrt{\frac{k_B T \omega_y}{X^2 m_{eff} \omega_x^2 Q_y} \left[1 + \left(\frac{Q_y(\omega_y^2 - \omega_x^2)}{\omega_y \omega_x}\right)\right]^{-1}} \tag{2.5}$$

where $k_B = 1.380649 \times 10^{-23} J/K$ is the Boltzmann's constant, X is the drive mode displacement , m_{eff} is the effective mass, and T is the operating temperature. It has units of $^\circ/\sqrt{hr}$.

- **Bias Instability (BI)** is the rate at which the gyroscope measurement erratically changes over time and shows in the Allan Deviation plot as zero slope (Figure 2.3). In

the PSD plot (Figure 2.4), the in-run bias instability has a slope of -1. It has units of $°/hr$ [17].

- **Angle Drift** in the output of a rate-integrating gyroscope is related to the energy losses and the frequency asymmetries of the resonator. Based on the model derived in [18],

$$\dot{\theta} = -A_g\Omega + \frac{1}{2}\Delta\left(\frac{1}{\tau}\right)\sin 2(\theta-\theta_\tau) + \frac{1}{2}\Delta\omega\cos 2(\theta-\theta_\omega)\frac{Q}{E}, \tag{2.6}$$

where $\theta_\tau, \theta_\omega, E$, and Q denote the principal axes of damping and elasticity, and the energy and quadrature error, respectively. Parameters $\Delta\omega$ and $\Delta\left(\frac{1}{\tau}\right)$ are the frequency mismatch and damping mismatch caused by the fabrication imperfections, where $\Delta\omega = \omega_x - \omega_y$ and $\Delta\left(\frac{1}{\tau}\right) = \frac{1}{\tau_x} - \frac{1}{\tau_y}$. Thus, the anisodamping and anisoelasticity need to be minimized in order to reduce the quadrature effect and drift of the output measurement.

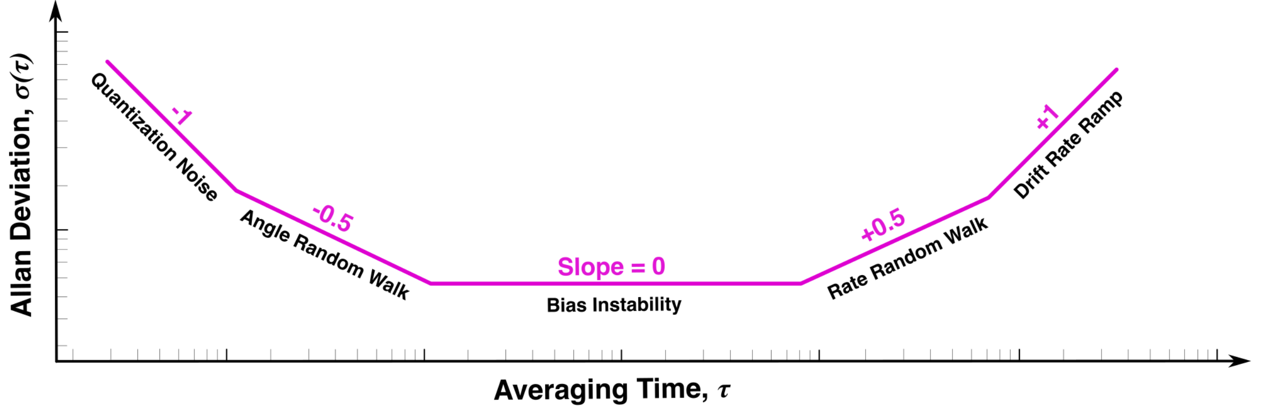

Figure 2.3: A schematic illustration of an Allan Deviation plot in log-log scale [1].

As made evident from the parameters affecting the performance of a CVG, a high Q-factor, damping symmetry, and stiffness symmetry are desired to improve the performance in rate and rate-integrating gyroscopes. These are the parameters that will be optimized in this thesis.

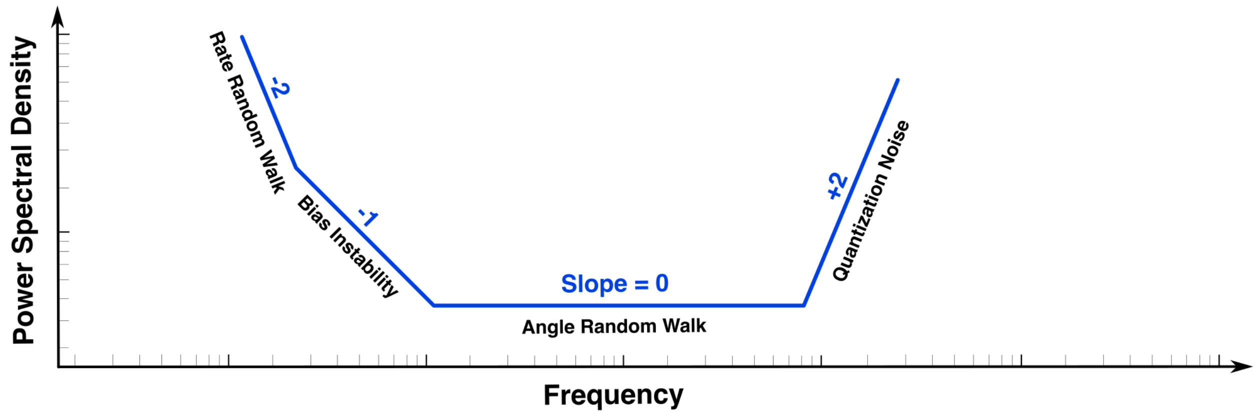

Figure 2.4: A schematic illustration of an PSD plot in log-log scale [2].

2.3 Energy Loss Mechanisms in MEM Resonators

Quality Factor is a figure of merit for energy preservation in resonators. The higher the Q, the less energy is lost each vibration cycle, which yields its formal definition:

$$Q = 2\pi \frac{\text{energy stored}}{\text{energy lost}} \tag{2.7}$$

The total Q-factor can be calculated form the reciprocal sum of the Q-factors from all of the damping mechanisms:

$$\frac{1}{Q_{\text{Total}}} = \frac{1}{Q_{\text{Air}}} + \frac{1}{Q_{\text{TED}}} + \frac{1}{Q_{\text{Anchor}}} + \frac{1}{Q_{\text{Surface}}} + \frac{1}{Q_{\text{Internal}}} + \frac{1}{Q_{\text{Mode-mixing}}} + \frac{1}{Q_{\text{Akhiezer}}} + \frac{1}{Q_{\text{Electrical}}} \tag{2.8}$$

which makes the weakest link dominate the overall Q-factor of the resonator [19], thus the importance of minimizing each energy loss mechanism individually. A brief introduction will be given for each of the major energy loss mechanisms in MEMS:

- **Viscous Air Damping** is one of the major sources of energy dissipation in MEMS, because micro-scale structures tend to have large surface-to-volume ratio and narrow

spacing between the fixed and movable parts. It is generally classified into two categories: squeeze film damping [20; 21] and lateral damping [22]. It makes it necessary to operate and package devices in ultra-high vacuum if high quality factors are desired, such as in the case for MEMS gyroscopes.

- **Thermoelastic Damping (TED)** is generated from the deformation of the vibrating structure creating gradients of heat between cold and hot regions, as is natural from the relationship between strain and temperature [23]. A general expression for the Q_{TED} of a vibrating beam can be found as [24]:

$$Q_{TED} = \frac{C_v}{\alpha^2 E T_0} \frac{1 + (\omega_0/\omega_R)^2}{\omega_0/\omega_R} \quad \text{where} \quad \omega_0/\omega_R = \frac{\chi \pi^2}{b^2}, \tag{2.9}$$

  This equation, although defined for a beam, gives an insight into the key parameters affecting TED for any resonator. α is the Coefficient of Thermal Expansion (CTE), E is the Young Modulus, C_v is the heat capacity, T_0 is the average temperature, ω_0 is the resonant frequency, and ω_R is the thermal relaxation rate. χ is the thermal diffusivity of the solid and b is the width of the beam. Therefore, both material selection and geometric design can impact TED.

- **Anchor Losses**. In any vibrating structure, there exist points of maximum displacement (anti-nodes) and fixed points (nodes) [25]. The structure is fixed to a substrate at its nodes, where displacement is zero but stress from the vibrational motion is applied. These stresses generate acoustic waves which dissipate into the substrate, taking energy away from the resonator. Techniques for minimizing anchor loss include anchor isolation (by means of geometric features or dissimilar materials), balanced vibration mode-shapes (so that stresses cancel each other out) and mode-shape optimization. The latter will be heavily studied in this thesis.

- **Surface Losses** comes from a non-ideal surface of a resonator. Many factors such

as surface roughness, surface oxidation, thin-film coatings, dust, moisture absorption, and sub-surface damage, influence surface condition and can reduce the quality factor of the resonator [26; 27; 28].

- **Internal Losses** are caused by the imperfections inside the material, such as defects, impurities, and grain boundaries. Therefore, high material purity is needed to reduce internal losses and achieve a high quality factor [29].

- **Mode-mixing** in a MEMS resonator would result in energy distribution from the actuated operational mode to all the nearby parasitic modes [30]. Large frequency separation between modes is desired to maintain quality factor.

- **Akhiezer Losses** arises from phonon scattering processes within the devices which is independent of structural geometry and more dominant in the resonators of high frequencies. An analytical expression for quality factor of Akhiezer limit in cubic semiconductor and dielectric crystal was provided in [31]:

$$f \cdot Q = \frac{3\rho c^2}{2\pi\gamma_{eff}^2 C_v T \tau_t} \tag{2.10}$$

  Where ρ is the material's density, c is the velocity of the acoustic wave, C_v is the heat capacity at constant volume, τ_t is the thermal phonon relaxation time, and γ_{eff} is the effective Grüneisen parameter. An estimation of $f \cdot Q = 3.2 \times 10^{13}$ is given in [32] for Quartz. This is presumed to be similar to the limit of Fused Silica, which would put the $Q_{Akhiezer}$ limit of the 30 kHz resonators in this work at 1000 Million.

- **Electrical**. Capacitive excitation and sensing of resonators is known to introduce damping forces [5]. Low resistance paths and appropriate actuation scheme help mitigate this source of energy loss [33].

2.4 The Dual-Shell Resonator Gyroscope (DSG)

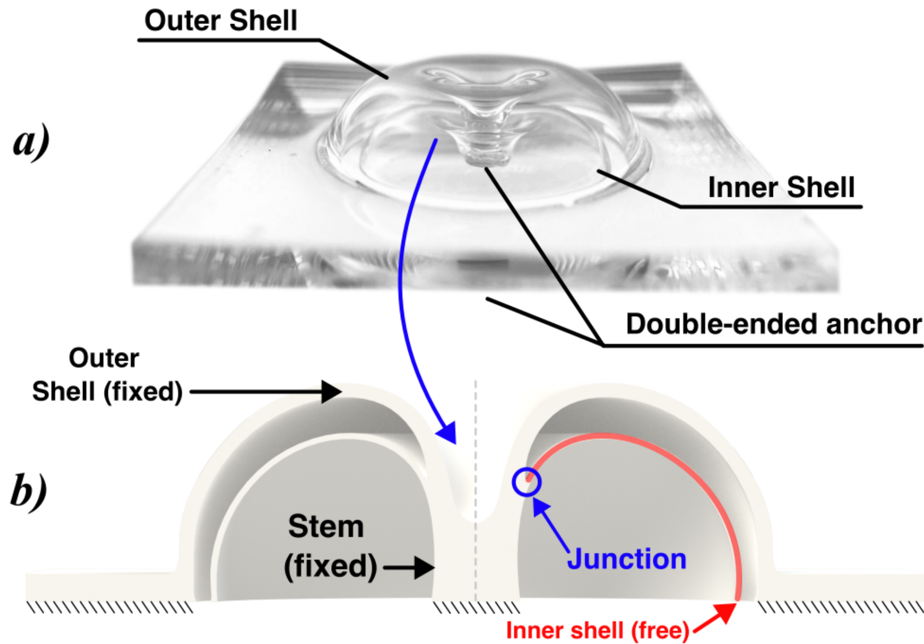

Figure 2.5: Photograph of Fused Silica Dual-Shell resonator. a) Stem and outer shell serve as a double-ended anchor, b) The junction (blue) is where the outer shell and stem connect to the inner shell (red).

The Dual-Shell resonator consists of a double-layer micro glassblown shell structure: an outer shell that serves both as an anchor and a protective casing to a vibrating inner shell (Figure 2.5). Such architecture has inherent benefits for continuous operation through mechanical shock and in adverse environments.

The principle of operation of the gyroscope is based on the inertial properties of elastic waves generated at the degenerate wineglass modes of vibration. When the vibrating inner shell is subjected to an external rotation around its revolution axis, the vibration pattern would precess with respect to the gyro case frame [10]. Figure 2.6 illustrates eight (out of many) vibrational modes of a typical dual-shell resonator. For gyroscope operation, the inner shell would operate in its degenerate wineglass modes, using excitation and detection scheme such as capacitive drive and sense [34], piezoelectric excitation [35], or optical detection [36]. The outer shell and the inner stem are anchored to a substrate, providing an double-end anchor

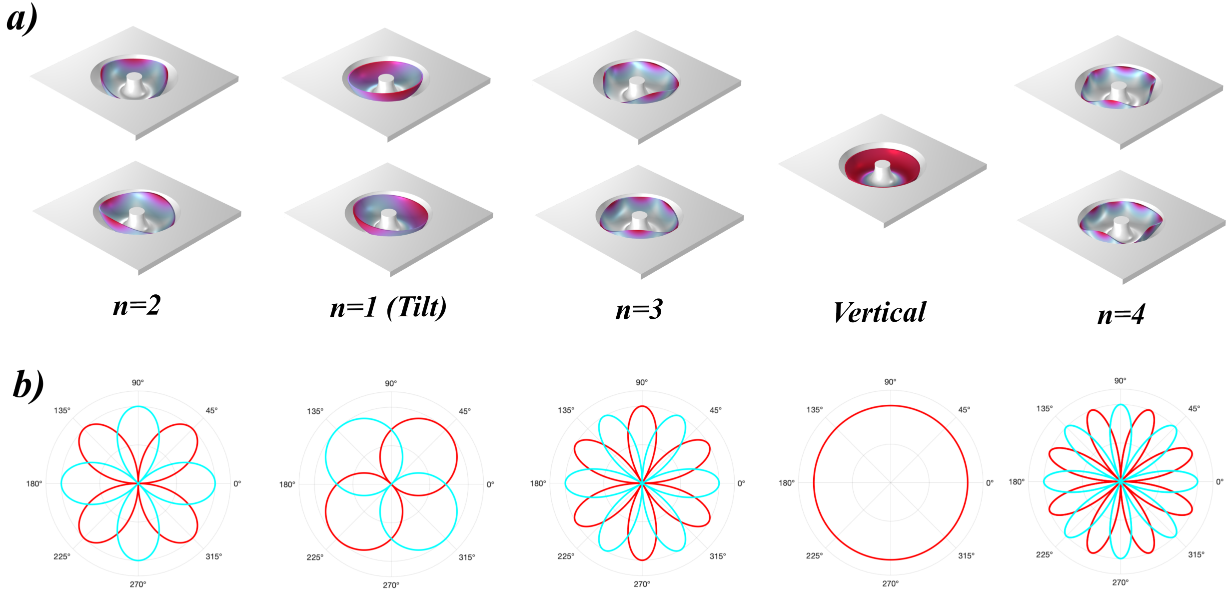

Figure 2.6: a) The first five vibrational modes of a typical Dual-Shell Resonator. b) Respective mode shape of out-of-plane displacement. The n=2 wineglass mode is preferable due to a higher angular gain in whole-angle operation.

to enhance the structural rigidity and shock survivability. Moreover, spurious modes, such as tilt, rotation, and out-of-plane motions, can be selectively stiffened through geometric design to reduce the environmental sensitivity and energy loss through mode mixing [30].

A triple-stack micro-glassblowing technique has been developed to fabricate Fused Silica (FS) Dual-Shell resonators and was initially reported in [37]. Using this approach, cavities were pre-etched on the "cap" and "device" wafers of fused Silica in an isotropic wet etching process using the HF solution. An evolution of this process reported in [38] switches cavities from the "device" to the "substrate" wafer, with the objective of keeping the sensing element pristine and free from any etching. This is the process that has been used for the fabrication of Dual-Shell Resonators in this thesis, and the steps of the process are shown in Figure 2.7.

The process starts with high-purity FS wafers (Corning HPFS® 7980) with nominal initial thicknesses of $500\mu m$, $150\mu m$, and $2mm$ as the cap, device, and substrate layers, respectively, Step (a). A layer of $2\mu m$ undoped polysilicon was deposited as a hard mask on the cap and

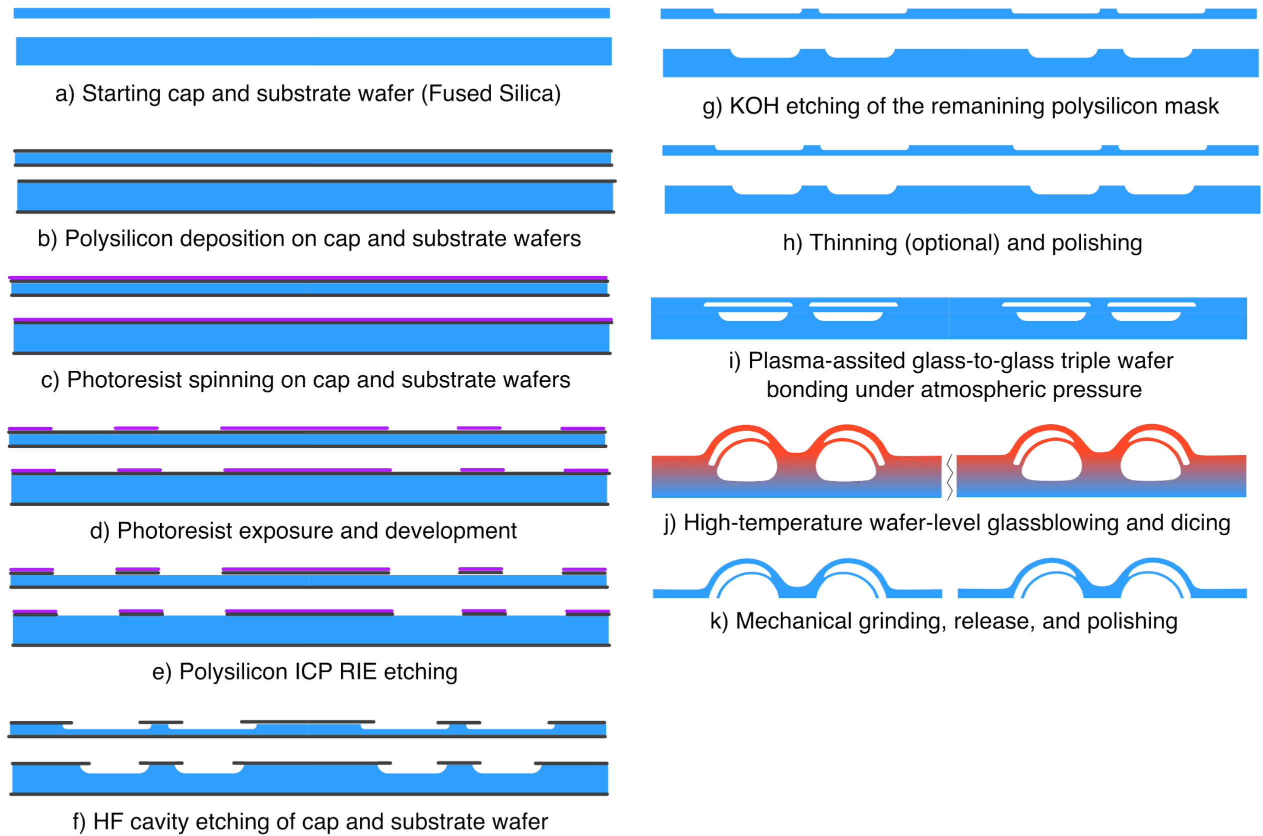

Figure 2.7: Fabrication process for Dual-Shell resonators [3].

substrate wafers, Step (b). Donut-shaped openings were lithographically patterned on one of the sides of this hard mask using Reactive Ion Etching (RIE), Steps (c), (d), and (e). The cap and substrate wafers are then submersed in Hydro-Fluoric (HF) acid (48% in water solution) for isotropic etching to create the cavities, Step (f). Cavities are around 100 m deep for the cap wafer and 300 m deep for the substrate, requiring up to 4-5 hours of etching. Then, polysilicon mask is removed in KOH solution, step (g), and wafers are polished and cleaned with Piranha, RCA-1, Acetone, and IPA, aligned, and bonded using plasma assisted glass-to-glass fusion bonding, trapping air inside the donut cavities at room temperature and pressure, Steps (h) and (i). Wafers were diced, and glassblowing was performed individually for each die in a Rapid Thermal Processing (RTP) furnace, Step (j). Finally, the inner device shell of the Dual-Shell was released by back-grinding and polishing, Step (k). Performing the glassblowing and release of the process on the die-level is optional, and the process is

compatible with the wafer-level batch fabrication.

These steps complete fabrication of the Dual-Shell resonator (Fig. 2.5a). For driving and sensing of the resonator and using it as a gyroscope, additional fabrication and assembly steps are required. Current implementations range from piezoelectric film deposition on the outer shell for excitation [35] or metallization of inner shell and bonding to an electrode substrate for capacitive driving and sensing [34].

Chapter 3

Low-Stress Topology Design for High Quality Factor

This section discuses anchor losses as the critical source of energy loss to be addressed. A parametric study is performed using FEM software to understand the origin of anchor losses, find optimal design trends, and define fabrication parameters of devices. The devices were fabricated and tested, showing good agreement with the predicted trends.

3.1 Quality Factor

Macro-Scale HRG technology sets the performance standard to achieve, with exceptional mechanical quality factors of over 25 Million which are used for the world's best gyroscopes [10]. Fabrication of macro-scale HRGs is based on individual machining of devices, something unfeasible for micro-scale HRGs because of the small tolerances required, and also undesirable for cost-effective gyroscopes. Micro-scale fabrication of high-Q hemispherical shells can be divided into two approaches: blow-torching and wafer-level glassblowing methods.

In the blow-torching process, high-purity fused silica substrates are clamped against a graphite fixture with pre-defined annular cavities, and while a high temperature (2500°C) flame hits and softens the glass from the back, vacuum is pulled inside the cavities and the glass molds into the fixture [39]. Afterwards, shells are mechanically lapped and polished. This process has been used to produce 10 mm diameter "Birdbath" resonators up to 12.5 Million at 13 kHz, and 5 mm diameter of 6 Million at 9 kHz [40]. For these resonators, TED is not expected to be the limiting factor ($Q_{TED} > 50 Million$) as long as the thickness of the rim is not critically small [41]. Anchor Loss was comprehensively studied in [42], yielding that thin and large shells are preferable for lower anchor losses, as well as thin long stems and overall small and stiff attachment to a substrate. All of these features are however not desirable for shock survivability and robustness of the gyroscope.

Despite not being limited by TED or anchor losses, blow-torched resonators in the cm-scale don't fully reach the quality factor of macro-scale HRGs. Looking at the remaining energy loss mechanisms, one unclear contributor is surface loss, which becomes ever more dominant as devices are scaled down due to the unfavorable increase in surface-to-volume ratio. Effects such as moisture absorption, surface roughness, subsurface damage, scratches, cleanliness, and thin-film coating friction, are challenges that must be accounted for and tackled. Dual-Shell resonator architecture is well suited for this thanks to the extra protection of the vibrating element.

Glassblowing on the micro-scale [6] as a fabrication process was first introduced in [7]. As discussed in section 2.4, cavities are etched on glass wafers and air is sealed inside. When the stack is introduced in a high-temperature furnace, glass becomes a highly viscous fluid and air expands to form 3D shell geometries. Quickly cooling the structure keeps the shell geometry from deflating. This process can create pristine, low-roughness glass shell structures which are potentially symmetric thanks to the balance of pressure and surface tension forces. Using the glassblowing process, hemispherical resonators were fabricated out of a combina-

tion of Pyrex Glass and silicon DRIE-etched cavities, achieving exceptional symmetry but with low potential for high quality factor due to the lower TED limit of Pyrex [8]. Fused Silica hemispherical shells were fabricated with quality factors up to 1.7 Million after thermal annealing, showing the importance of thermal shock stress relief after the glassblowing process [9]. The Dual-Shell architecture was introduced in [37] with potential advantages over the "single-shell" design, such as inherent protection from the environment for the sensing element, particularly during handling, and robust double-ended anchor. Quality factor up to 1.8 Million at 4 kHz and around 10 mm in diameter after annealing were measured [11]. A study performed on the effect of Dual-Shell geometry on anchor losses showed that a relationship might exist between junction stresses and anchor loss [12], but devices were not optimized at the point of the study. Therefore, it's expected that with adequate design, quality factor of these devices can be pushed further.

3.2 Energy Loss Mechanisms

As introduced in section 2.3, total quality factor of the Dual-Shell resonator is defined by:

$$\frac{1}{Q_{\text{Total}}} = \frac{1}{Q_{\text{Air}}} + \frac{1}{Q_{\text{TED}}} + \frac{1}{Q_{\text{Anchor}}} + \frac{1}{Q_{\text{Surface}}} + \frac{1}{Q_{\text{Internal}}} + \frac{1}{Q_{\text{Mode-mixing}}} + \frac{1}{Q_{\text{Akhiezer}}} + \frac{1}{Q_{\text{Electrical}}} \quad (3.1)$$

As a starting point for the design of new high-Q devices, non-limiting mechanisms are ruled out:

- Viscous air damping is eliminated by operating resonator in ultra-high vacuum of 0.1μTorr.
- Resonators are tested with piezoelectrical shaker excitation and optical read-out, so no damping forces from a capacitive interface exist. Therefore, electrical damping is not

present.

- Akhiezer losses for silicon and glass MEMS resonators were estimated in [43]. A $Q \cdot f$ factor of 3.2×10^{13} is expected, which for the resonant frequency of 30 kHz of the devices in this study, yields $Q_{\mathrm{AKE}} \approx 1000$ Million.

- Likelihood of internal losses are minimized by using high purity Fused Silica, and all resonators are annealed using thermal profiles from [44] to ensure cooling stresses from the glassblowing process are eliminated.

- Mode-mixing is avoided through FEM eigenfrequency analysis during the design phase. Several kHz separation is ensured between wineglass and spurious modes.

- Thermoelastic Damping (TED) limit is inherently high due to the low CTE and thermal conductivity of Corning 7980 Fused Silica. Despite this, certain geometry features such as a thin rim could decrease it significantly. For this reason, TED limit is verified with FEA Software COMSOL Multiphysics [45], and it is found to be $Q_{\mathrm{TED}} > 100$ Million.

- Surface losses are challenging to quantify. Multiple contribution from different phenomena can overlap. A standard post-fabrication cleaning procedure is performed on all resonators [46]:

  1. Acetone soak to remove wax after release process.
  2. Solvent Clean.
  3. 30 minute Ultrasonic DI water bath.
  4. Nitrogen gun blow drying.
  5. 30 minute $100°C$ hotplate drying.
  6. 30 minutes Piranha (2:1 H_2SO_4/H_2O_2) Clean.
  7. Nitrogen gun blow drying.
  8. 30 minute $100°C$ hotplate drying.

9. 30 minutes RCA1 (5:1:1 DI Water/H_2O_2/NH_4OH) Clean.
10. Nitrogen gun blow drying.
11. Anneal
12. Characterization

This procedure ensures proper cleaning while eliminating all moisture and stresses on the last step, the anneal, after which any kind of water soaking must be avoided. However, this procedure hasn't been exhaustively optimized, and it is not for certain that all surface losses are eliminated. Nevertheless, the results of this work show that anchor loss is dominant in most devices and to the very least, this post-processing defines a common surface loss limit for all devices.

Assuming these contributions have been eliminated or minimized, only anchor losses remain to be addressed.

3.3 Design for Low Anchor Loss

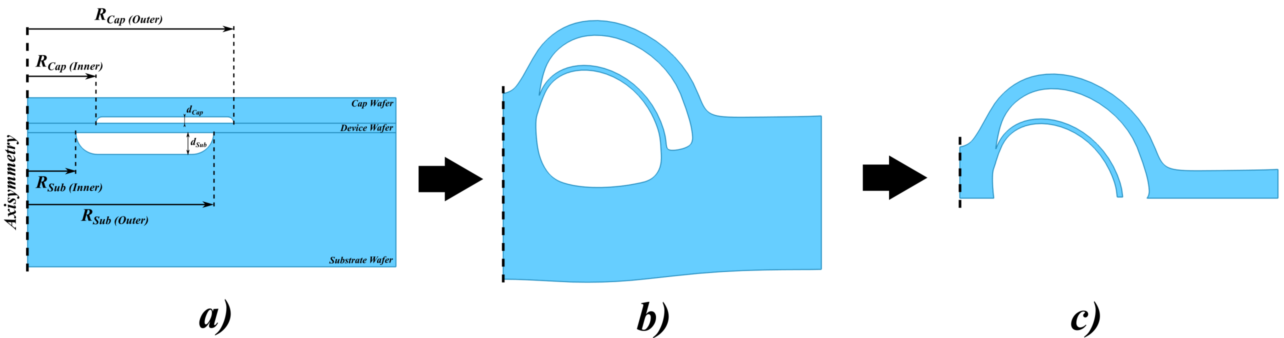

Figure 3.1: Schematic of how Dual-Shell Geometry is predicted during design process. a) Dimensions of the donut cavities etched into glass during the wet etching step. b) During glassblowing simulation, the depth, size and relative position between the cavities generate a unique Dual-Shell geometry. c) Grinding and polishing remove material and only the final resonator is left behind.

The geometry of the Dual-Shell resonator is defined by the size of the cavities etched in the glass (Figure 3.1a). After glassblowing, the cavities expand and create the characteristic two-shell geometry (Figure 3.1b). After removing the back bulk of material, the inner resonator is free to vibrate (Figure 3.1c). For given wafer thicknesses and glassblowing temperature, the cavities etching depth directly controls the height of the resonator, and the radius of the cavities and their relative position define key characteristics in the geometry, such as the junction position (Figure 2.5b). By changing the junction position, a clear set of topologies ranging from fully hemitoroidal to hemispherical shells is obtained (Figure 3.2).

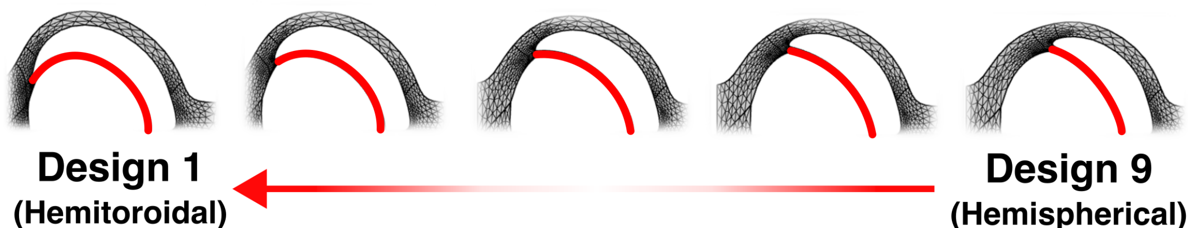

Figure 3.2: A family of topologies were considered, where inner-shell geometry (red) changes from hemispherical (rightmost) to hemitoroidal (leftmost).

To isolate and study the effect of topology on anchor losses, all other geometry parameters are kept equal between designs: stem radius, shell radius, and rim thickness (Table 3.1). This can be accomplished by keeping cavity depth and cavity radius equal for all designs except for the inner radius of the cap wafer cavity.

Parameter	Rim Radius	Outer Height	Rim Thickness	Die Radius
Value	2.75 mm	2 mm	100 μm	5.5 mm

Table 3.1: Geometric parameters and their values that were kept constant in all considered topologies.

3.4 Anchor Loss Simulation

Design process for Dual-Shell resonators starts with a glassblowing model to predict the final geometry of the structure based on the parameters in Figure 3.1a. This model is built

in COMSOL Multiphysics software [45] and is an evolution of the one presented in [9] and consists of a non-isothermal viscous glass flow considering convection heat transfer from the furnace environment to an individual Dual-Shell die. Adiabatic expansion is assumed for the trapped air. The obtained mesh is then saved for subsequent simulations, such as TED and anchor losses.

Anchor Loss simulation is a field to which significant efforts have been devoted with the objective to understand and better predict what has been found to be a critical source of energy loss for MEMS devices [47]. However, as accurately portrayed in [43], typical Perfectly Matched Layer (PML) anchor loss simulations are not reliable, and small changes in meshing or geometry can yield vastly different quality factors. Simply predicting Q_{Anchor} with a simulation is not a good design approach, which is made even more evident by how boundary conditions and attachment methods have been found to experimentally affect anchor losses [48].

However, PML simulations can be used to compare different design variations relative to each other, which is the objective of this study. As will be shown in the results, several orders of magnitude improvement can be observed between designs, while keeping all other parameters of the simulation unchanged.

In the anchor loss model, a dual-shell structure is anchored to a substrate made of the same material as the device, Corning 7980 Fused Silica. Simulation with dissimilar substrate material is beyond the scope of this study. The substrate has an semi-spherical geometry with three distinct areas of meshing. The first layer has the same radius as the die of the device, and the Dual-Shell Resonator is anchored both at the stem and outer shell regions. The second layer is a buffered region of substrate which, if made several times larger than the wavelength of the acoustic waves, allows for visualization of acoustic wave propagation before entering the Perfectly Matched Layer, a sign that the simulation is converged [47] (Figure 3.3a). The third and final layer is the PML, which absorbs acoustic waves emitted

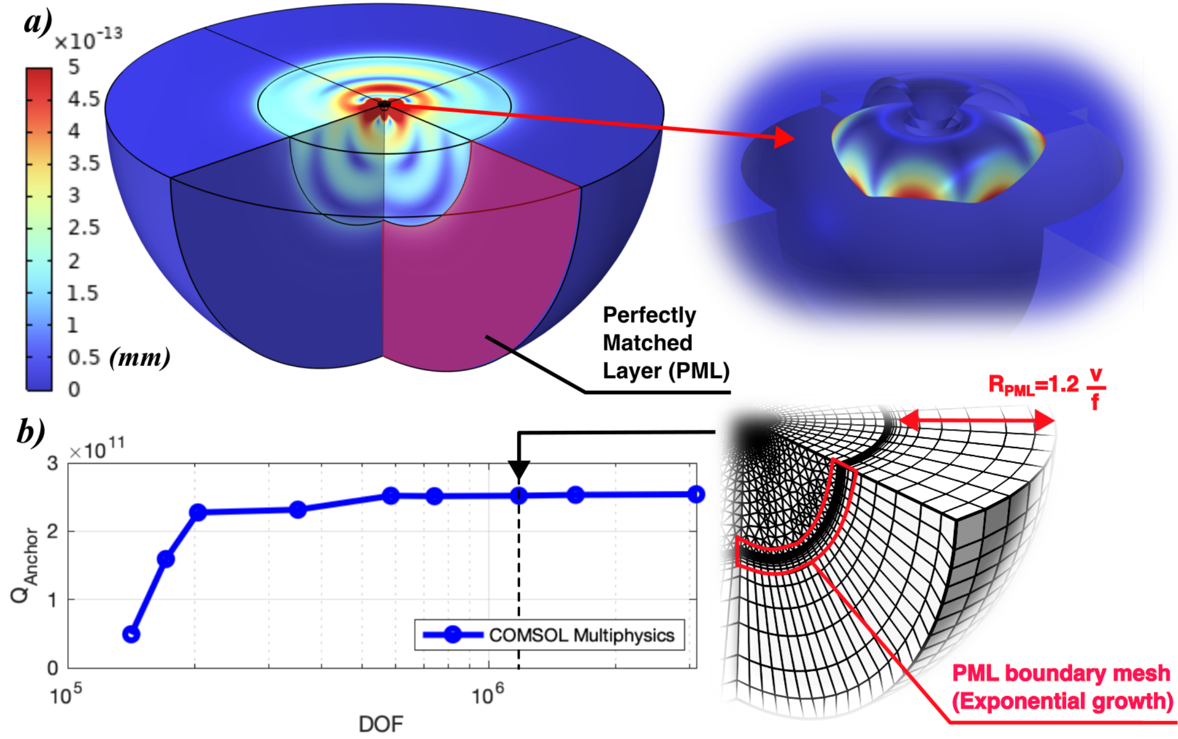

Figure 3.3: Simulation of anchor losses. a) A spherical Perfectly Matched Layer (PML) absorbs acoustic waves and is used to estimate energy lost from the resonator through attachment. b) Mesh convergence plot. ∼1.5 million DOF (right) was used for all simulations.

from the device without reflection. The width of the PML was selected 20% larger than the wavelength of the acoustic waves to ensure the waves decay completely. The scale factor of PML was set to 1. To confirm convergence of the simulation, mesh densities with different number of Degree of Freedom from 150 thousand to 3 million were tested, showing the quality factor converges with the selected mesh size (∼1.5 million of degrees of freedom) (Figure 3.3b).

3.5 Simulation results

A parametric sweep covering geometries from hemitoroidal to hemispherical shells was simulated. In Figure 3.4a, Q_{Anchor} predicted by the simulation is plotted against the design

number, showing a clear trend of better performance for fully hemitoroidal shells for n=2 mode. For n=3, a maximum in Q_{Anchor} was found between hemispherical and hemitoroidal shells (Figure 3.4b). To better understand the origin of this behavior, in-plane and out-of-plane stress at the junction was plotted against design number for both primary wineglass modes, n=2 and n=3 (Figure 3.5).

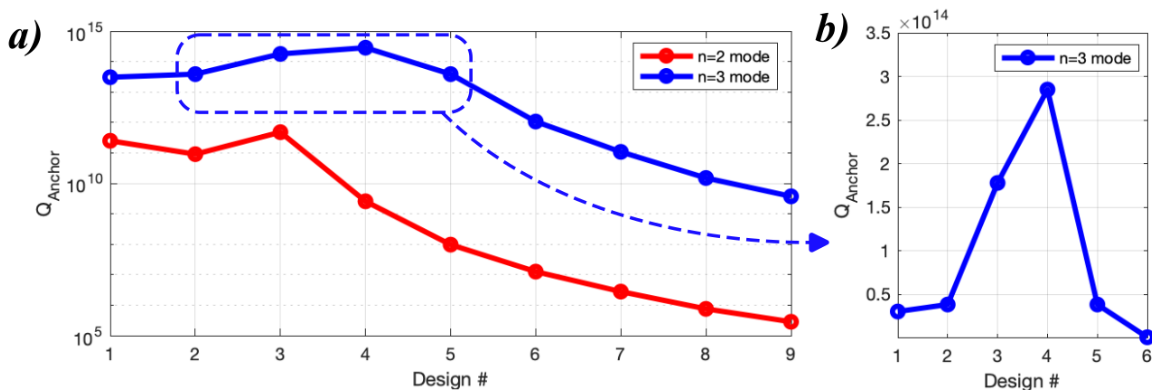

Figure 3.4: a) FEA results for Q_{Anchor} for different topologies. Hemitoroidal shells (Designs #1-3) are found to have higher Q_{Anchor} limit than hemispherical shells (Designs #7-9). b) Close-up results for n=3 mode, where a maximum is found for Design #4.

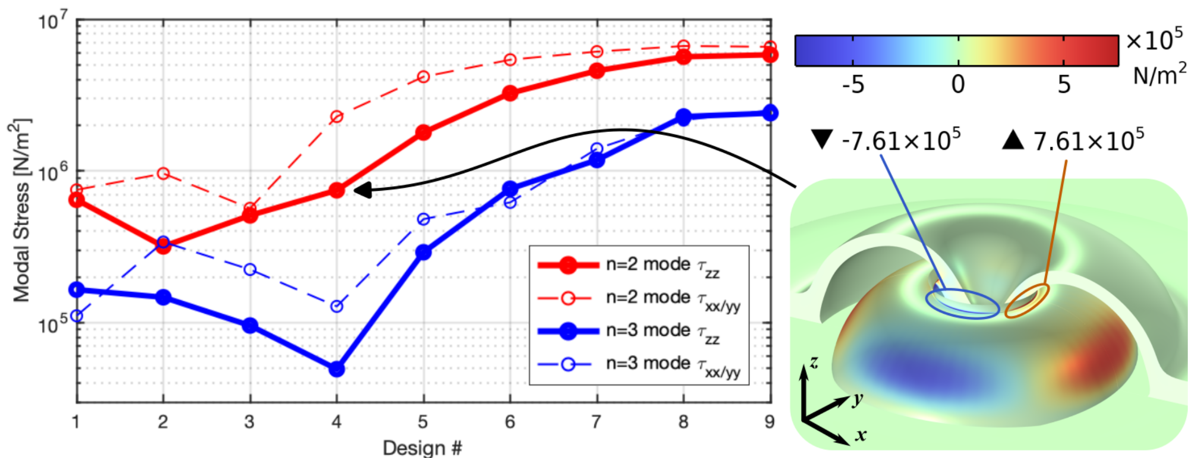

Figure 3.5: Modal stress tensor components as a function of design topology. Modal stresses are automatically normalized by FEA software. Identical trends were found for out-of-plane stress (this figure, solid lines) and Q_{Anchor} (Fig. 4) in both n=2 and n=3 modes.

Flat MEMS gyroscopes operating in wineglass mode, such as Toroidal and Disk Resonator Gyroscopes, operate in a mode-shape that is fully symmetric and balanced both in-plane and out-of-plane [49]. In these cases, anchor-loss can originate from asymmetries in real

devices leading to unbalanced in-plane and out-of-plane stress resultants at the anchor, or the crystal-orientation dependent mechanical properties of certain types of anisotropic Silicon [50].

However, the three-dimensional geometry of an HRG means that, even if a device is fully symmetric with respect to the axis of revolution and is made of an isotropic material (such as Fused Silica), unbalanced out-of-plane stress still exists. The magnitude of the out-of-plane stress has been found to vary with geometry (Figure 3.5), and it was at its minimum for hemitoroidal topology for n=2. For n=3 mode, a minimum is found for Design #4. Based on this, a compromise exists between maximizing Q_{Anchor} for n=2 or n=3 mode.

In addition, in-plane stress shows a similar trend as out-of-plane for both modes. Minimizing in-plane stress can be beneficial for lowering the impact of asymmetries in Quality Factor.

Finally, stresses have been found to be overall lower for n=3 mode compared to n=2, which can be related to the overall higher quality factor in n=3 mode that is predicted in the anchor-loss simulation and that is usually seen in fabricated devices.

3.6 Fabrication of resonators

Devices were fabricated with the process described in section 2.4. High-purity Corning HPFS® 7980 Fused Silica wafers with thicknesses of $500\mu m$, $150\mu m$, and $2mm$ were used as the cap, device, and substrate wafers, respectively. The layer of $2\mu m$ undoped polysilicon was deposited using LPCVD. A $8\mu m$ positive photoresist layer was spin-coated and then exposed using a Karl Suss Mask Aligner. After development, the exposed polysilicon was etched with a Trion Technology ICP/RIE. Cavities in the glass were time-etched at a rate of 1.35 μm/min in 48% Hydrofluoric Acid. After this, polysilicon mask was removed in an 8M KOH solution, and wafers were polished on the cavities side. Then, wafers were cleaned in

Piranha (2:1 H_2SO_4/H_2O_2) and RCA1 (5:1:1 DI Water/H_2O_2/NH_4OH) solutions. Finally, the surfaces to be bonded are plasma activated in a Trion Technology ICP, exposed to running DI water for 2 minutes and nitrogen blow dried. For the alignment sensitive bond of cap/device stack to substrate wafer, a Idonus Sarl MAS+DIM Shadowmask Aligner was used. Bonds were annealed for 24 hours at room temperature followed by a 450 °C anneal for 48 hours. For glassblowing step, an MTI KSL-1700X-KA Box furnace with a custom sliding shuttle for Rapid Thermal Processing (RTP) was used. Glassblowing temperature was set at $1600°C$. Back-grinding and polishing release was performed using Allied High-Tech Multi-Prep System. Finally, devices went through the post-fabrication cleaning and conditioning procedure described in section 3.2.

3.7 Characterization of devices

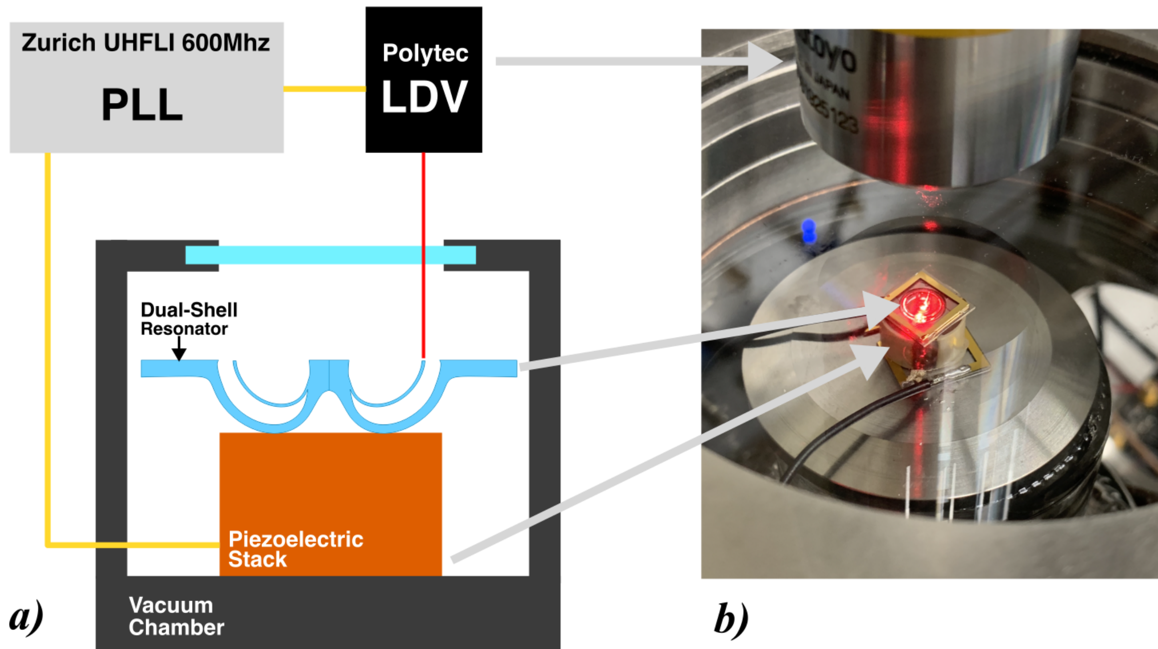

Figure 3.6: a) Schematic of experimental setup showing Dual-Shell resonator inside vacuum chamber for characterization. b) Picture of setup in laboratory during Dual-Shell characterization.

For characterization of resonant frequencies and quality factor, Dual-Shell resonators are placed upside down, laying on the outer-shell, on top of a piezoelectric shaker. A vertical displacement of the shaker on the order of a few nanometers is used to excite wineglass modes, which are detected through velocity measurements on the rim using a Laser Doppler Vibrometer (PolyTec Inc.). A Phase Locked Loop (PLL) is implemented with a Zurich Instruments UHF Lock-In Amplifier, and ring-down measurements of quality factor are taken in a vacuum environment. The experimental setup is illustrated in Figure 3.6.

Figure 3.7 shows all measured quality factors for 33 devices, ordered from highest to lowest. The resulting plot matches the expected results, with device ordering from design #1 (highest Q) on the left of the plot, design #5 in the middle, and design #9 (lowest quality factors) on the right. Certain variability exist within each group, in particular for designs #5 and #9 devices, where Q can sometimes overlap in between both groups. This can be attributed to abnormally high frequency mismatch in the resonators, which is known to make the wineglass mode less balanced leading to higher anchor losses. In contrast, design #1 average higher quality factor in n=2 mode independent from frequency symmetry, and the same happens in n=3 mode for design #5 resonators. This can be attributed to the minimization of in-plane stresses as well as out-of-plane that was predicted in Figure 3.5.

Highest recorded quality factor for the optimal design #1 resonators is 3.9 Million in n=2 mode, a >50% increase compared to previous, larger size Dual-Shell resonators. Consistently achieving $\sim$ 3 Million quality factor on the optimized devices confirms the effectiveness of topology focused design.

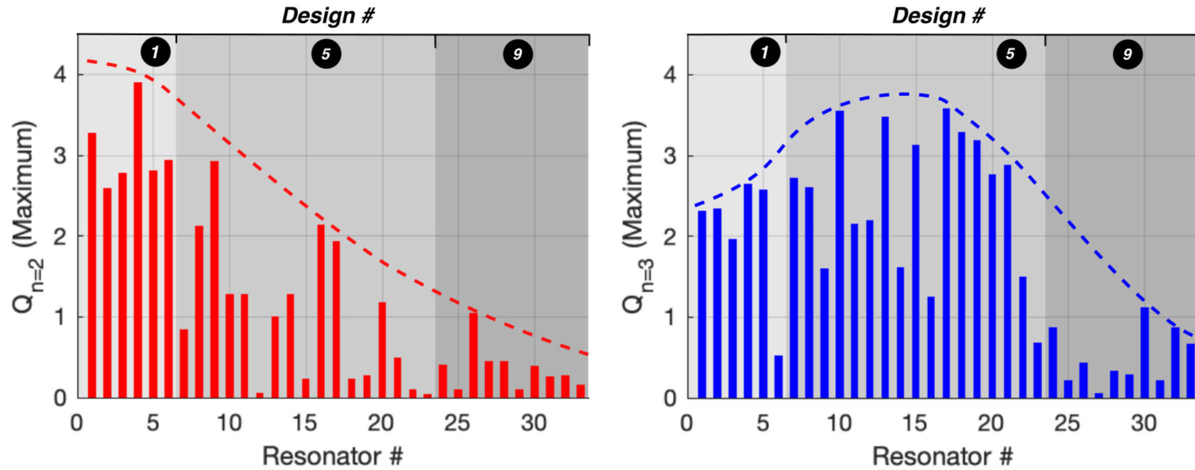

Figure 3.7: Experimental quality factor (maximum of the two degenerate modes) in n=2 (left, red) and n=3 (right, blue). Dashed lines were manually fitted to showcase trends from Figure 3.4. Resonators are ordered from low frequency mismatch (left) to high (right) within each design.

3.8 Conclusions

In this section, the current status of quality factor of micro-scale Hemispherical Resonators has been analyzed. Blow-torching of hemispherical resonators in the cm size have achieved quality factors on the order of 12 Million. In comparison, glassblown resonators were previously limited to 1.8 Million. Through stress minimization at the anchor point, topologies for high-Q anchor limit have been found and fabricated. The optimal designs feature higher quality factor compared to those without optimization, as predicted by FEA PML anchor loss simulations. Highest measured quality factor was 3.9 Million. However, despite the increase in quality factor, a Q-factor and symmetry gap still exists between blow-torching and Dual-Shell resonators. This can be attributed to aspect ratio of the inner shell (low height) or surface losses, issues that should be at the forefront of the future work on quality factor improvement of Dual-Shell resonators.

Chapter 4

Identification of Structural Imperfections

This section introduces a method to model structural asymmetries present in 3D Glassblown Fused Silica Dual-Shell micro-scale hemispherical resonator Gyroscopes (DSG). The method is based on acquisition of a sequence of high-magnification images which are digitally stitched together to create a combined high-resolution view of the critical features of the DSG. These images are then used to identify and measure structural asymmetries, which are subsequently used to construct a solid 3D model of the resonator with imperfections and followed by a Finite Element Method (FEM) analysis. Frequency mismatches of five devices were used to demonstrate the method, confirming to accurately predict mismatches -varying from 100 to 1000 Hz- for both n=2 and n=3 wineglass modes. The method presents a non-contact approach for studying the effect of non-idealities in the fabrication process, with the end goal of mitigating them and increasing the symmetry yield and quality of devices.

4.1 Frequency Symmetry

The exceptional performance achieved by macro-scale Hemispherical Resonator Gyroscopes (HRG) [10] has motivated the effort to fabricate these devices on the micro-scale, while maintaining their geometry and characteristics [51], [52]. However, the limited tolerances of traditional micro-fabrication techniques pose a challenge when building 3D micro-structures that meet the required precision and symmetry of high-performance rate-integrating gyroscopes. In conventional MEMS fabrication, imperfections in the lithography, etching, and morphology of the structural material would typically define asymmetries [53]. However, the mechanisms defining asymmetries in the wafer-level glassblowing process are different [7; 6].

The Fused Silica (FS) Dual-Shell micro-scale HRG (DSG) is a novel implementation of the hemispherical resonator concept, showing potential for extremely high quality factor and continuous operation despite mechanical shock, vibrations, radiation, and harsh thermal conditions. The Dual-Shell resonator fabrication process was disclosed in [3] and first demonstrated in [37]. Even though glassblowing on the micro-scale does not fundamentally suffer from traditional sources of asymmetry due to its nature [8], it can introduce new dependencies such as temperature non-uniformity during glassblowing, preferential glass flow relative to gravity, and others. Previous work on glassblown hemispherical resonators, [54], focused on imperfections introduced during the grinding release process, showing that these can cause frequency mismatches on the order of tens of Hz, which can be corrected using directional grinding. It has been shown that Dual-Shell Resonators can achieve low frequency mismatch of only a few Hz as-fabricated, [11]. However, an occasional appearance of larger mismatches, above 100 Hz, was not well understood. Identifying and understanding the source of large asymmetries is critical to increasing yield and quality of the wafer-level fabrication process.

In this section, we report a method to optically identify, measure, and model structural

asymmetries present in the geometry of micro-fabricated DSG. Accurate prediction of a wide range of frequency mismatches demonstrates the effectiveness of this method, providing an insight into possible causes of the asymmetries.

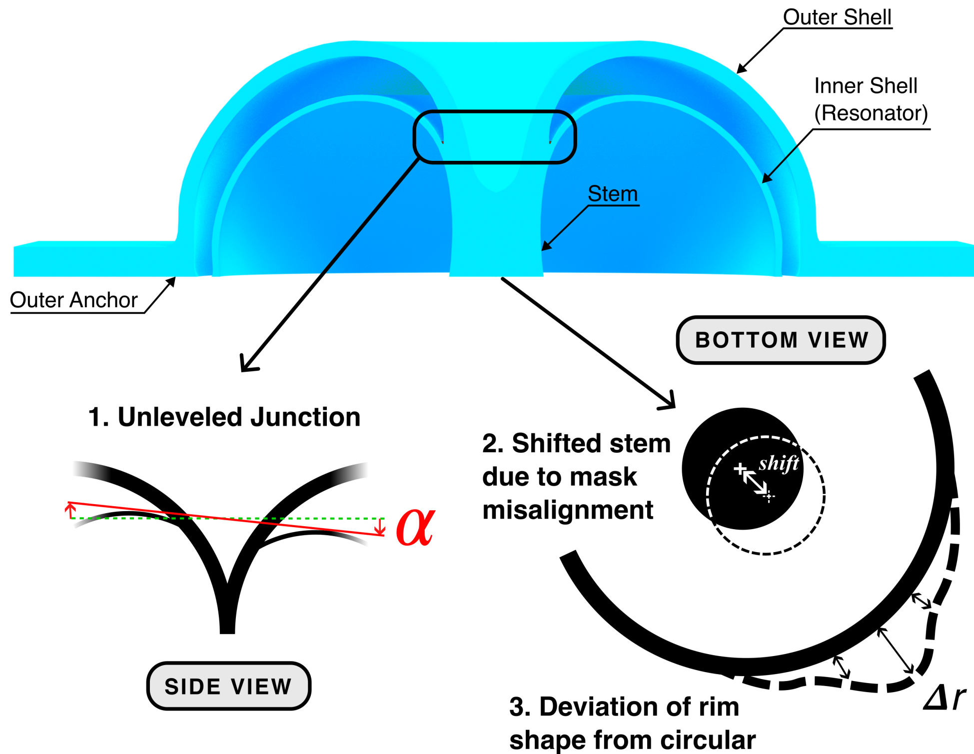

Figure 4.1: Three types of asymmetries considered in this study.

4.2 Method

The Dual-Shell architecture includes an outer shell that serves both as an anchor and a protective casing to the vibrating inner shell (Fig. 4.1). Such architecture increases robustness of the structure to external shock, shielding it from the environment. However, the multi-shell architecture also makes analysis of the resonator geometry a complex task, due to light reflections, transparency of the material, and the view of the inner shell being obscured from most viewing angles.

To overcome these metrology challenges, devices were analyzed by a high-magnification digital microscope from below (bottom view) and perpendicular to the structure (side view), Fig. 4.1. The hemispherical resonators used for this study had a device radius of 2.7 mm and rim thickness on the order of 100 μm. For each device, multiple high-magnification (50x), high-resolution (1.17 pixels/μm) images of the inner shell rim were acquired using a Leica DM6 B digital microscope with Differential Interference Contrats (DIC) and digitally stitched together using matching features (Fig. 4.3a). Then, these images were processed using a metrology software from Leica Application Suite (LAS X) to reveal structural asymmetries. In this step, three types of asymmetries were considered: deviation of the rim shape from circular, a shifted stem, and an unleveled junction (Fig. 4.1). Deviations of the rim from circularity can be expressed as the changing value of the radius along the symmetry axis of the shell, and this is the first time they were studied. A shifted stem was also studied in [42] for its role in anchor losses, and it is defined as a misalignment between the center of the stem and the center of circumference of the rim. For micro-scale hemispherical resonator gyroscopes, tilting is mainly associated with non-uniform temperature distribution during glassblowing [54] or blow-torching [55]. To measure tilting of the junction, lower resolution side-view images were acquired (Fig. 4.3b). From this viewing angle, the tilt was observed through the transparent outer-shell.

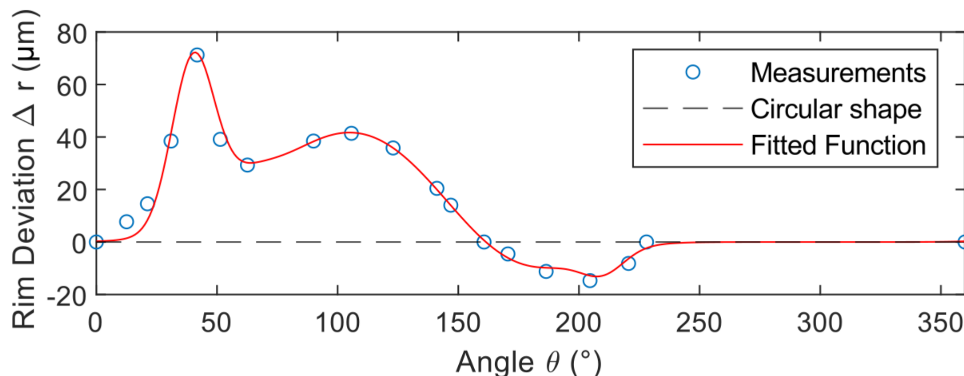

Figure 4.2: Rim deviation function fitted to measurements for subsequent importing to FEM model. All five devices exhibit similar deviations in varying magnitudes. Device #1 is shown for illustration purpose.

In particular, discrete measurements of rim deviations were fitted to functions of the form:

$$\Delta r(\theta) = \sum_{n=1}^{N} A_n sin(\theta/2 + s_n)^{k_n}, \tag{4.1}$$

where θ is the angle along the central axis of symmetry, A_n is amplitude of the radius error in micrometers, s_n is an angular shift, and k_n is an exponent to tune the sharpness of the deformation. The form of these functions should not be confused with a Fourier transform, which would contain multiple harmonics. The exponential sinusoidal terms were chosen based on their ability to represent aberrations in the radial profile of the rim, thus matching the measurements obtained from metrology when multiple terms are combined (Fig. 4.2).

The value of each asymmetry was introduced into a parametric finite element solid model in COMSOL Multiphysics software, [45]. The values were applied as prescribed displacements to a symmetric solid 3D model (Fig. 4.4) obtained from glassblowing simulations, using a non-isothermal glass flow model similar to the one used in [5]. Finally, the asymmetric mesh was exported for subsequent frequency mismatch simulation. The simulation consisted of a solid-mechanics eigenfrequency analysis with the outer anchor and the stem as boundary conditions (fully clamped). It was observed that an insufficiently dense mesh would introduce artificial frequency split in FEM simulations. Therefore, an adequate meshing of the model of $\sim$ 400,000 degrees-of-freedom was verified by computing the frequency degeneracy when asymmetries are not present, yielding an accuracy of ± 1 Hz. A higher accuracy can be obtained with a denser mesh, but it wasn't necessary for the magnitude of mismatches considered in this study.

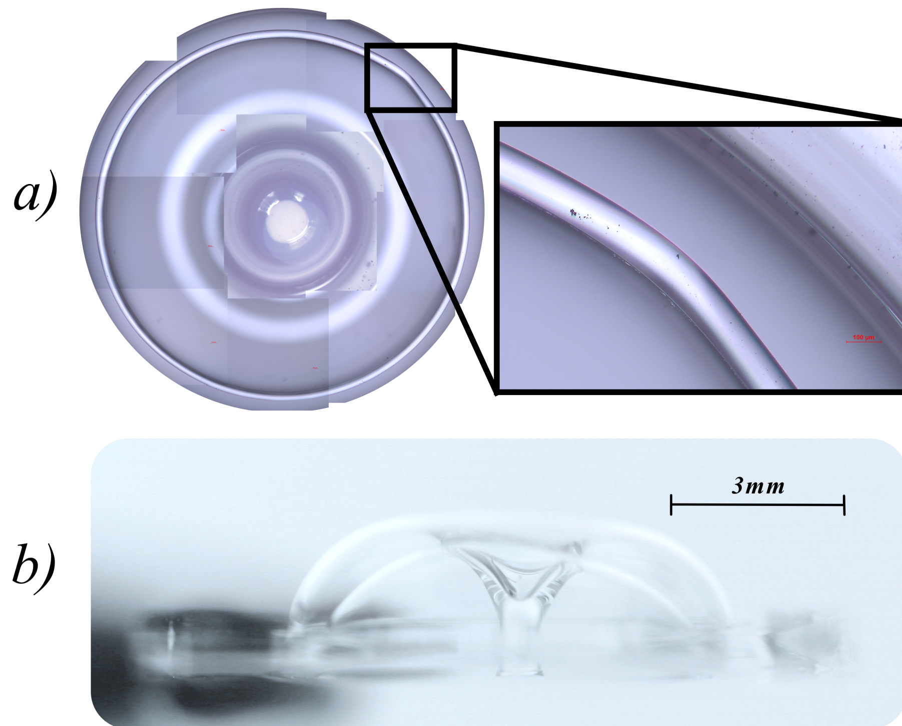

Figure 4.3: a) Bottom view (Fig. 4.1) of the rim of DSG resonator. Images are manually stitched into position using overlapping features. b) Side-view of the resonator, where tilt of the junction can be observed and measured.

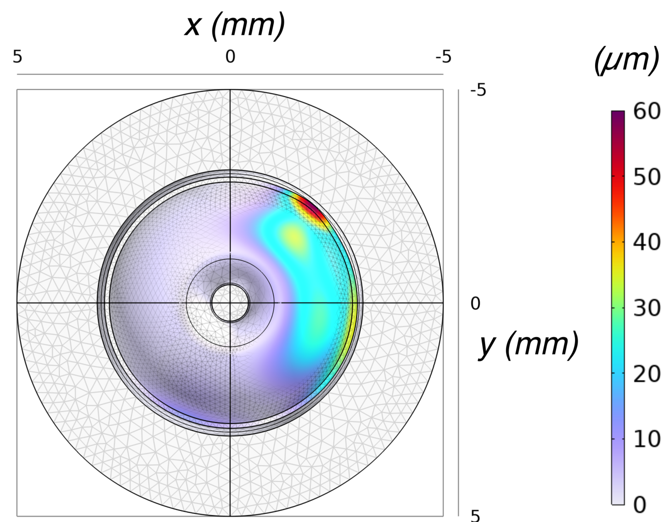

Figure 4.4: Identified rim imperfections in device #1 transferred to a solid model: the asymmetric COMSOL mesh was used for subsequent frequency analysis. The legend illustrates deviation from an idealized, perfectly symmetric DSG structure.

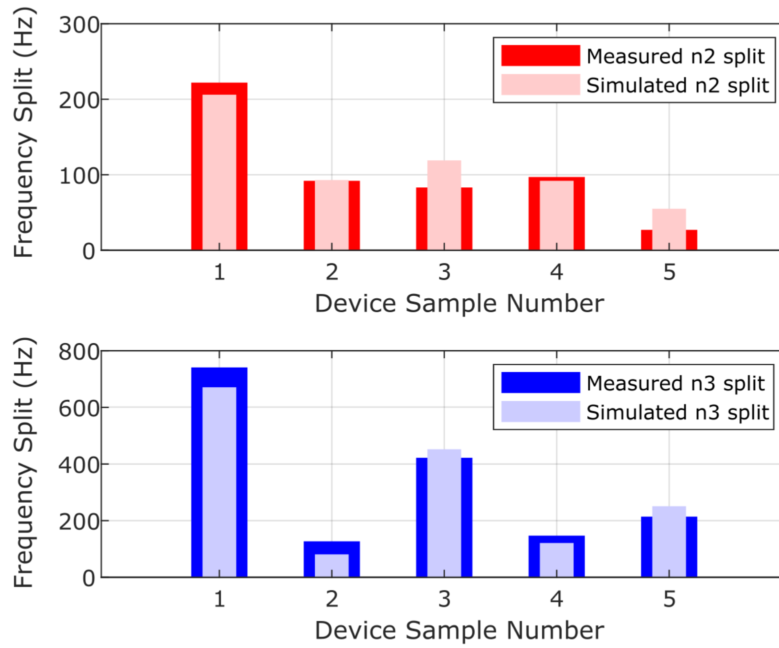

Figure 4.5: Measured and simulated frequency mismatch for n=2 and n=3 wineglass modes. The method was applied to a wide range of frequency mismatches.

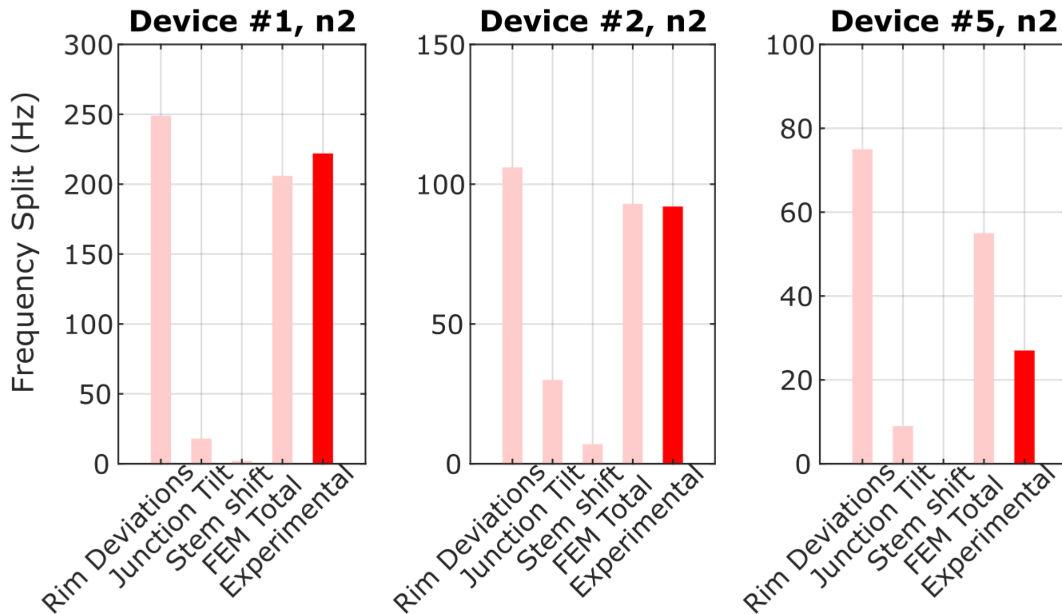

Figure 4.6: Decomposition of the simulated frequency splits into the different asymmetry types for n=2. For n=3, it was found that the only contributing asymmetry was the deviations of the rim shape from circular.

4.3 Simulation and Experimental Results

The frequency mismatches of five different devices were used to demonstrate the methodology. The samples were experimentally analyzed using Laser-Doppler Vibrometry, and compared to the FEM simulation of structures with imperfections. Resonators with varying levels of asymmetry were considered, ranging from 10 to 1000 Hz (Fig. 4.5).

The FEM modelling approach allowed to look at the relative contribution of each type of asymmetry individually. Fig. 4.6 shows the frequency split of each device with only one of the asymmetries considered. First, the analysis shows that the asymmetry type generating the most mismatch is the rim deviations from the circular shape, followed by the junction tilt. The stem shift contribution was observed to have a minimal effect. Second, the analysis shows the inter dependencies between asymmetries. Based on their relative orientation (i.e. direction of tilting), the defects can significantly amplify or cancel out each other, and therefore cannot be considered independently.

Finally, it has been analytically predicted [44], and shown experimentally [55], that only asymmetry deviations (radius, thickness) of 4th and 6th harmonics will contribute exclusively to frequency degeneracy of n=2 and n=3 wineglass modes, respectively. Fig. 4.7 shows the harmonic content of each of the functions (Eq. 4.1) fitted to the radius variation across each of the devices. As shown, 4th (red regions) and 6th (blue regions) harmonics are present in the error functions. This highlights the necessity to improve the fabrication process to eliminate the corresponding sources of asymmetry which, while random in nature, can introduce 4th and 6th order harmonics and lead to large frequency mismatches.

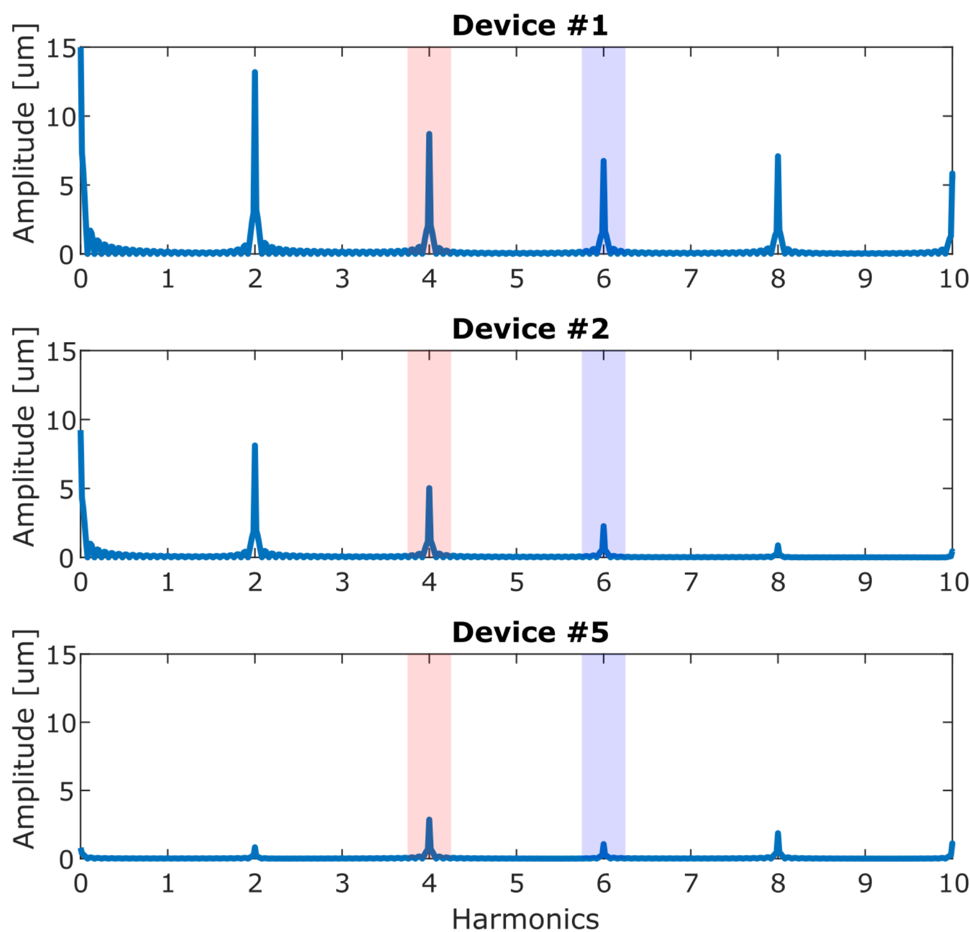

Figure 4.7: Harmonic content of the functions fitted to radius deviations. Only the 4th and 6th harmonics contribute to frequency split for n=2 and n=3, respectively, and are highlighted by red and blue regions on the plot.

4.4 Conclusions

In this study, a modeling approach aided by optical metrology was shown to be a powerful tool for identification of imperfections causing both large and small frequency degeneracy in 3D shell resonators. The identified asymmetries were shown to be the major contributions to mismatch of the fabricated devices, particularly radial deviations and junction tilt. The FEM method allowed to decouple sources of asymmetry, showing how they can have a cancelling effect on each other based on their relative orientation. It was also shown that even localised

radial deviations can introduce 4th and 6th harmonic error, known to be direct cause of fundamental degeneracy, highlighting the importance of improving fabrication tolerances to yield low-mismatch devices that make-up gyroscopes with higher sensitivity and reduced drift.

Chapter 5

Future Work

In the previous chapter, structural asymmetries that can lead to large frequency mismatches have been identified. However, their origin remains unknown. Each of these asymmetry types needs to be linked to non-idealities during fabrication in order to know how to increase the yield of the wafer-level process. Below are some of the hypothesis to be investigated.

5.1 Radial deviations

The radial deviations have been identified to be the primary fabrication error in glassblown devices. A closer look at the fabricated wafer stack before glassblowing has shed light on the origin of these imperfections. Fig. 5.1b shows high-resolution SEM pictures of the cavities etched on the glass using isotropic hydrofluoric acid etching. This is a critical step that defines the geometry of the resonator. Large spherical-shaped imperfections can be observed on the rim of the cavities, hinting at a deficient masking of the 2 μm polysilicon layer.

The reason why the acid has penetrated the mask is not fully understood, but it is believed that the large undercuts created during the needed long isotropic etching times (to depths

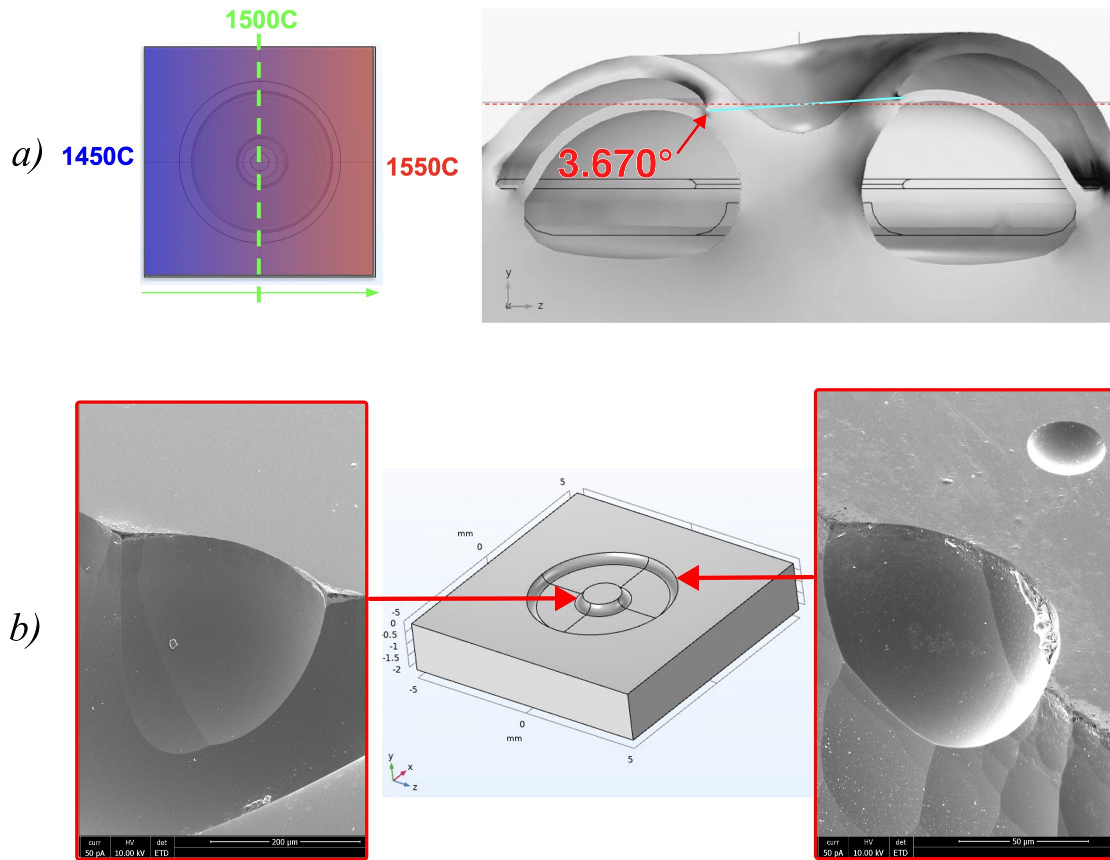

Figure 5.1: a) Left: temperature gradient used as an input to the 3D Glassblowing simulation. Right: resulting geometry of a Dual-Shell highlighting the exaggerated junction tilt. b) Left/Right: SEM images of defects in the glass caused by deficient masking during hydrofluoric acid etching. Center: schematic view of a typical etched donut cavity for Dual-Shell fabrication.

between 300 and 400 μm) can be partly the reason. After a large undercut is created, a large portion of the 2μm mask remains hanging over the rim of the cavity, and pre-stress from deposition can cause to crack or break in this area. This is analogous to a really thin and long cantilever breaking at its anchor point. This would explain how large imperfections appear only around the edges of the cavities, but not anywhere else around the same wafer.

Glassblowing simulations of such imperfections show that they can lead to radial deviations, such as the ones measured in the fabricated devices presented in Chapter 4.

5.2 Junction tilt

The tilting of the junction was observed in the Dual-Shell resonators when both the inner and outer shells are tilted in the same direction as from the side-view (Fig 4.3b). This tilt has been shown to introduce a significant mismatch for n=2 wineglass mode, but not for n=3.

Temperature non-uniformity during glassblowing has been considered a likely source of tilt for glassblown resonators in recent work [54]. Simulations that consider a non-uniform temperature field across the device show how a gradient of $50°C$ of the $1500°C$ glassblowing process can lead to 3-4 degrees of tilting, in line with what has been observed in the fabricated devices (Fig. 5.1a). To correct this, a custom furnace with higher temperature uniformity is being developed to address the challenge of uniformity.

In addition to temperature non-uniformity, bonding non-uniformity has been identified as a likely source of tilt for wafer-level glassblown resonators. In step (i) of the fabrication process (Fig. 2.7), glass wafers with cavities are bonded using fusion bonding. This process, while having the advantage of being interface-free (no extra material is used which could diffuse into the glass or fail during glassblowing), is known to be prone to yield issues, as it is extremely sensitive to the cleanness of the interface and the timing of the process [56]. Small unbonded spots on a wafer can create bubbles during glassblowing and slightly deform geometry in a non-significant way. However, if large areas remain unbonded, air will escape during glassblowing, a shell structure will not be formed and glassblowing will fail altogether.

In between these two cases, there exist a possibility that a cavity is sealed but partially bonded, sometimes as few as tens or hundred of micrometers along the edge of the cavity (Fig. 5.2a). As air expands and pushes to separate surfaces during glassblowing, this bond non-uniformity will lead to a deformed geometry.

To showcase the effect of this non-ideality on junction tilt, the effect of a bonding non-uniformity was simulated in a 3D glassblowing model for cap wafer and substrate wafer cavities, showing a direct relationship with tilt of the inner-shell (Fig. 5.2c).

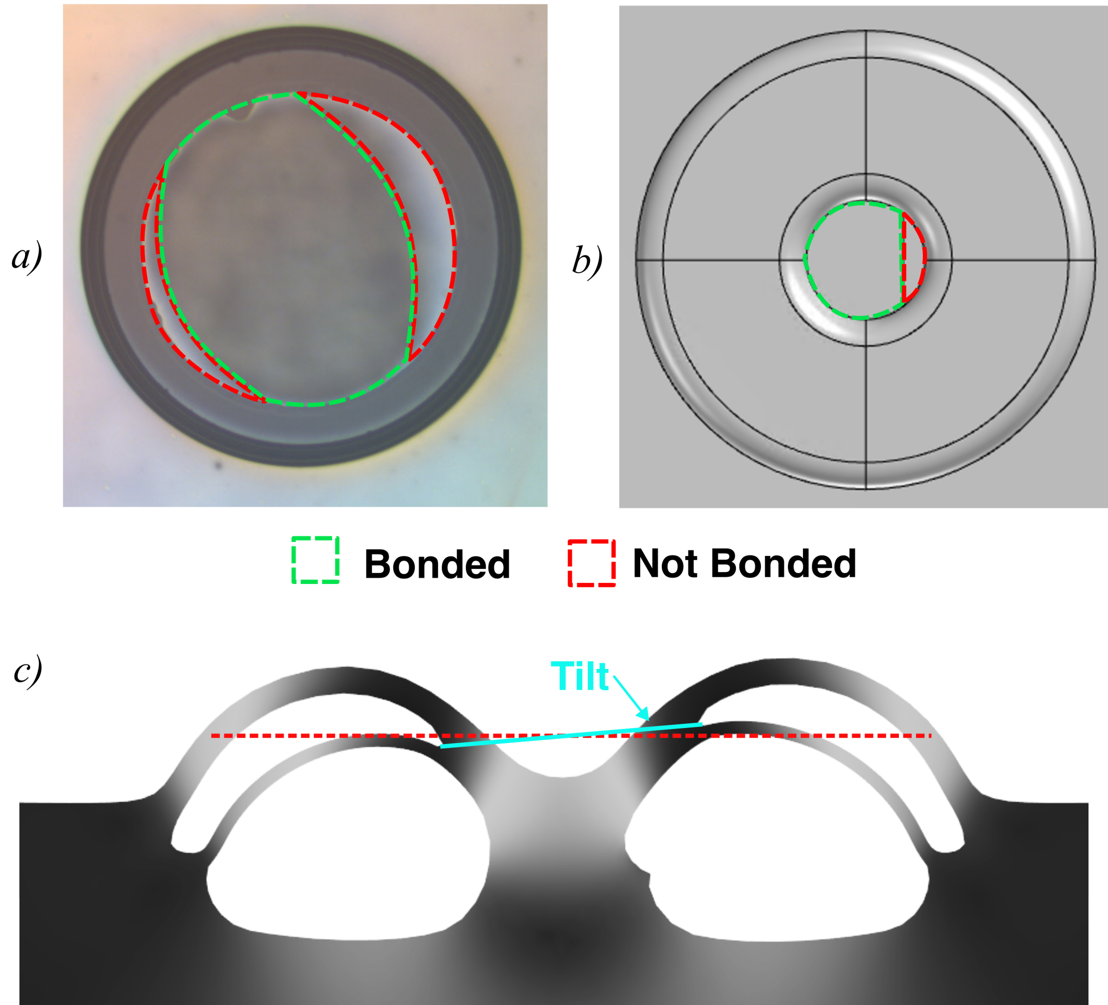

Figure 5.2: a) Polarization sensitive microscope picture, where bonded areas appear solid in color (green outline) and not bonded areas are detected as color gradients (red outline). b) Geometry setup of the cavity for the FEM 3D glassblowing simulation. c) Simulation showing tilting of the inner shell as a result (cyan).

5.3 Stem shift

Although shifts in position of the stem have been shown to be a small contributor to the total symmetry mismatch of devices, the cause of this imperfection will be evaluated for reasons beyond frequency degeneracy, such as precise bonding of the stem to an electrode substrate [34], or its possible effect on the anchor loss [42].

Misalignment between wafers of the stack during the plasma-activated bonding could introduce this type of shifting. However, the bonding misalignment of the fabricated devices was measured before glassblowing to be well below the measured shifts, on the order of 5 μm, as opposed to stems being shifted by as much as 100 μm, in some cases. Not all devices feature this type of imperfection, which would be expected to affect uniformly the whole wafer if it were an alignment-related issue.

Therefore, the most likely cause of shifting and overall stem deformation is hypothesized to be due to non-uniformity of stem bonding, exacerbated by etching related imperfections, like the ones shown in Fig. 5.1b.

5.4 Suggested improvements to fabrication

Different approaches are being considered to remove most sources of asymmetry:

- Improvements to Polysilicon masking. Up to date, a 2μm doped polysilicon hard mask has been used for Dual-Shell fabrication with deficient results due to imperfections, as explained in this work. Due to the apparent relationship between stress of the overhang created and imperfections, thicker masks in addition to post-deposition annealing could prevent the hard mask from failing.

- Define cavities in Fused Silica by using Femtosecond-Laser Induced Chemical Etching (FLICE) [57], a new micro-fabrication paradigm likely to offer increased resolution and selectivity of etching for the cavities.

- Improvement of fusion bonding. The origin of bonding non-uniformity should be further studied. Addition of thin films on the interface that can enhance the bond without significantly changing material composition have been studied in literature [56].

- Higher temperature and/or higher glassblowing time. Surface tension forces will work towards a symmetric structure if given enough time for structure to develop its shape.

Chapter 6

Conclusions

In this work, two key aspects of fundamental performance of glassblown resonators for Dual-Shell Gyroscopes have been comprehensively studied: quality factor and frequency symmetry. Through meticulous experimental characterization and thorough FEM multi-physics simulations, each chapter delves into issues and solutions to maximize performance in these micro-scale devices, while also expanding the knowledge on solid-mechanics behavior of highly symmetric and low loss MEM resonators.

- Chapter 2: The basic concepts of Coriolis Vibratory Gyroscopes were introduced, as well as the theoretical basis and relevance of two key performance parameters, mechanical quality factor and frequency symmetry. Then, the concept, geometry, and fabrication of Dual-Shell Gyroscope was presented.
- Chapter 3: A comprehensive study of the effect of topology on anchor losses of the Dual-Shell resonator was performed, and optimized devices were fabricated and achieved quality factors up to 3.9 Million, more than a 50 % compared to previous results. By understanding the relevance of out-of-plane stresses in complex 3D resonators, this approach demonstrated the importance of minimizing modal stresses at the anchor to

achieve high quality factors.

- Chapter 4: This chapter presented a method for identifying the imperfections in geometry causing large and small frequency mismatch in Dual-Shell resonators. Frequency mismatches of five devices -varying from 100 to 1000 Hz- were accurately predicted. The modeling approach allowed to observe separately the effect of three different types of imperfections, as well as how they can impact the degeneracy of n=2 and n=3 modes differently.

- Chapter 5: The three main types of imperfections were studied from a fabrication point of view, linking them to non-idealities introduced during the fabrication process. This serves as a basis for the suggestion of process improvements and changes that could improve resonator symmetry in future devices.

As a result, the research presented in these chapters contributes to the knowledge of how higher performance Dual-Shell Resonator Gyroscopes can be designed and fabricated. Improved quality factor and frequency symmetry of resonators lay the foundation for achieving low drift and highly sensitive gyroscopes on the micro-scale and with low power consumption.

Bibliography

[1] "IEEE Standard Specification Format Guide and Test Procedure for Linear Single-Axis, Nongyroscopic Accelerometers," *IEEE Std 1293-2018 (Revision of IEEE Std 1293-1998)*, pp. 1–271, Feb. 2019. [Online]. Available: https://ieeexplore.ieee.org/document/8653544

[2] "IEEE Standard Specification Format Guide and Test Procedure for Single-Axis Interferometric Fiber Optic Gyros," *IEEE Std 952-1997*, pp. 1–84, Feb. 1998. [Online]. Available: https://ieeexplore.ieee.org/document/660628/?arnumber=660628

[3] A. M. Shkel, M. H. A. Ardakani, and Y. Wang, "Fused quartz dual shell resonator and method of fabrication," US Patent US20 200 309 527A1, Oct., 2020.

[4] G. Langfelder, M. Bestetti, and M. Gadola, "Silicon MEMS inertial sensors evolution over a quarter century," *Journal of Micromechanics and Microengineering*, vol. 31, no. 8, p. 084002, Aug. 2021.

[5] M. Weinberg, R. Candler, S. Chandorkar, J. Varsanik, T. Kenny, and A. Duwel, "Energy loss in MEMS resonators and the impact on inertial and RF devices," in *International Solid-State Sensors, Actuators and Microsystems Conference (TRANSDUCERS)*, Denver, CO, Jun. 2009.

[6] E. J. Eklund and A. M. Shkel, "Self-inflated micro-glass blowing," US Patent US20 080 280 124A1, Nov., 2008. [Online]. Available: https://patents.google.com/patent/US20080280124A1/en

[7] ——, "Glass Blowing on a Wafer Level," *IEEE/ASME Journal of Microelectromechanical Systems*, vol. 16, no. 2, pp. 232–239, Apr. 2007.

[8] D. Senkal, M. J. Ahamed, A. A. Trusov, and A. M. Shkel, "Achieving Sub-Hz Frequency Symmetry in Micro-Glassblown Wineglass Resonators," *IEEE/ASME Journal of Microelectromechanical Systems*, vol. 23, no. 1, pp. 30–38, Feb. 2014.

[9] M. H. Asadian, Y. Wang, and A. M. Shkel, "Development of 3D Fused Quartz Hemi-Toroidal Shells for High-Q Resonators and Gyroscopes," *IEEE/ASME Journal of Microelectromechanical Systems*, vol. 28, no. 6, pp. 954–964, Dec. 2019.

[10] D. Rozelle, "The Hemispherical Resonator Gyro: From Wineglass to the Planets," *AAS/AIAA Space Flight Mechanics Meeting, Savannah, GA, USA*, Feb. 2009.

[11] M. H. Asadian, D. Wang, and A. M. Shkel, "Fused Quartz Dual-Shell Resonator Gyroscope," *IEEE/ASME Journal of Microelectromechanical Systems*, vol. 31, no. 4, pp. 533–545, Aug. 2022.

[12] W. Guan, D. Wang, M. H. Asadian, Y. Wang, and A. M. Shkel, "Effect of Geometry on Energy Losses In Fused Silica Dual-Shell Gyroscopes," in *IEEE International Symposium on Inertial Sensors and Systems (INERTIAL)*, Avignon, France, May 2022.

[13] A. M. Shkel, "Type I and Type II Micromachined Vibratory Gyroscopes," Apr. 2006, pp. 586–593. [Online]. Available: http://www.ion.org/publications/abstract.cfm?jp=p&articleID=6689

[14] D. D. Lynch, "Lynch (1998) - Coriolis vibratory Gyros.pdf," in *Symposium Gyro Technology*, Stuttgart, Germany, Sep. 1998, pp. 1–14.

[15] D. Vatanparvar and A. M. Shkel, "Quadrature-Induced Noise in Coriolis Vibratory Gyroscopes," in *2020 IEEE International Symposium on Inertial Sensors and Systems (INERTIAL)*, Mar. 2020, pp. 1–4. [Online]. Available: https://ieeexplore.ieee.org/document/9090022/?arnumber=9090022

[16] R. Leland, "Mechanical-thermal noise in MEMS gyroscopes," *IEEE Sensors Journal*, vol. 5, no. 3, pp. 493–500, Jun. 2005, conference Name: IEEE Sensors Journal. [Online]. Available: https://ieeexplore.ieee.org/document/1430703/?arnumber=1430703

[17] "IEEE Standard for Inertial Sensor Terminology," *IEEE Std 528-1994*, pp. 1–24, Aug. 1994. [Online]. Available: https://ieeexplore.ieee.org/document/392610/?arnumber=392610

[18] D. Lynch, "Vibratory gyro analysis by the method of averaging," St. Petersburg, Russia, 1995. [Online]. Available: https://www.scienceopen.com/document?vid=d12e66c2-0990-4050-ba12-3fee9e1a40ab

[19] V. Kaajakari, *Practical MEMS*. Small Gear Pub., 2009, google-Books-ID: nX5mPgAACAAJ.

[20] J. J. Blech, "On Isothermal Squeeze Films," *Journal of Lubrication Technology*, vol. 105, no. 4, pp. 615–620, Oct. 1983. [Online]. Available: https://doi.org/10.1115/1.3254692

[21] Q. Lu, W. Fang, C. Wang, J. Bai, Y. Yao, J. Chen, X. Xu, and W. Huang, "Investigation of a complete squeeze-film damping model for MEMS devices," *Microsystems & Nanoengineering*, vol. 7, no. 1, pp. 1–13, Jul. 2021, publisher: Nature Publishing Group. [Online]. Available: https://www.nature.com/articles/s41378-021-00279-6

[22] S. Azma, G. Rezazadeh, R. Shabani, and E. Alizadeh-Haghighi, "Viscous fluid damping in a laterally oscillating finger of a comb-drive micro-resonator based on micro-polar fluid theory," *Acta Mechanica Sinica*, vol. 32, no. 3, pp. 397–405, Jun. 2016. [Online]. Available: https://doi.org/10.1007/s10409-015-0550-2

[23] C. Zener, "Internal Friction in Solids II. General Theory of Thermoelastic Internal Friction," *Physical Review*, vol. 53, no. 1, pp. 90–99, Jan. 1938, publisher: American Physical Society. [Online]. Available: https://link.aps.org/doi/10.1103/PhysRev.53.90

[24] R. Lifshitz and M. L. Roukes, "Thermoelastic damping in micro- and nanomechanical systems," *Physical Review B*, vol. 61, no. 8, pp. 5600–5609, Feb. 2000, publisher: American Physical Society. [Online]. Available: https://link.aps.org/doi/10.1103/PhysRevB.61.5600

[25] Z. Hao, A. Erbil, and F. Ayazi, "An analytical model for support loss in micromachined beam resonators with in-plane flexural vibrations," *Sensors and Actuators A: Physical*, vol. 109, no. 1, pp. 156–164, Dec. 2003. [Online]. Available: https://www.sciencedirect.com/science/article/pii/S0924424703004898

[26] S. D. Penn, G. M. Harry, A. M. Gretarsson, S. E. Kittelberger, P. R. Saulson, J. J. Schiller, J. R. Smith, and S. O. Swords, "High quality factor measured in fused silica," *Review of Scientific Instruments*, vol. 72, no. 9, pp. 3670–3673, Sep. 2001. [Online]. Available: https://doi.org/10.1063/1.1394183

[27] J. Yang, T. Ono, and M. Esashi, "Surface effects and high quality factors in ultrathin single-crystal silicon cantilevers," *Applied Physics Letters*, vol. 77, no. 23, pp. 3860–3862, Dec. 2000. [Online]. Available: https://doi.org/10.1063/1.1330225

[28] J. Chu, X. Liu, C. Liu, J. Zhang, J. Xiao, X. Wang, X. Chen, and J. Xu, "Fundamental investigation of subsurface damage on the quality factor of hemispherical fused silica shell resonator," *Sensors and Actuators A: Physical*, vol. 335, p. 113365, Mar. 2022. [Online]. Available: https://www.sciencedirect.com/science/article/pii/S0924424722000036

[29] K. Numata, S. Otsuka, M. Ando, and K. Tsubono, "Intrinsic losses in various kinds of fused silica," *Classical and Quantum Gravity*, vol. 19, no. 7, p. 1697, Mar. 2002. [Online]. Available: https://dx.doi.org/10.1088/0264-9381/19/7/363

[30] D. Vatanparvar and A. M. Shkel, "Effect of fabrication imperfections on energy loss through mechanical mode coupling in MEMS," in *2018 IEEE International Symposium on Inertial Sensors and Systems (INERTIAL)*, Mar. 2018, pp. 1–2. [Online]. Available: https://ieeexplore.ieee.org/document/8358155

[31] S. S. Iyer and R. N. Candler, "Mode- and Direction-Dependent Mechanical Energy Dissipation in Single-Crystal Resonators due to Anharmonic Phonon-Phonon Scattering," *Physical Review Applied*, vol. 5, no. 3, p. 034002, Mar. 2016. [Online]. Available: https://link.aps.org/doi/10.1103/PhysRevApplied.5.034002

[32] S. Ghaffari, S. A. Chandorkar, S. Wang, E. J. Ng, C. H. Ahn, V. Hong, Y. Yang, and T. W. Kenny, "Quantum Limit of Quality Factor in Silicon Micro and Nano Mechanical Resonators," *Scientific Reports*, vol. 3, no. 1, p. 3244, Nov. 2013, publisher: Nature Publishing Group. [Online]. Available: https://www.nature.com/articles/srep03244

[33] D. Wang and A. M. Shkel, "Effect of EAM on Quality Factor and Noise in MEMS Vibratory Gyroscopes," in *2021 IEEE International Symposium on Inertial Sensors and Systems (INERTIAL)*, Mar. 2021, pp. 1–4, iSSN: 2377-3480. [Online]. Available: https://ieeexplore.ieee.org/document/9430471/?arnumber=9430471&tag=1

[34] D. Wang, M. H. Asadian, D. Hii, and A. M. Shkel, "Fused Silica Dual-Shell Gyroscope with In-Plane Actuation by Out-Of-Plane Electrodes Realized Using Glassblowing and Thru-Glass-Vias Fabrication," in *IEEE International Conference on Micro Electro Mechanical Systems Conference (MEMS)*. Tokyo, Japan: IEEE, Jan. 2022, pp. 154–157. [Online]. Available: https://ieeexplore.ieee.org/document/9699792/

[35] D. Wang, N. A. Strnad, Y. Wang, A. R. Parrish, R. R. Benoit, R. R. Knight, and A. M. Shkel, "Indirect Excitation of micro-HRG Using Segmented Piezoelectric ALD PHT Actuator," in *IEEE International Symposium on Inertial Sensors and Systems (INERTIAL)*. Lihue, HI, USA: IEEE, Mar. 2023, pp. 1–4. [Online]. Available: https://ieeexplore.ieee.org/document/10103950/

[36] P. Pai, F. K. Chowdhury, C. H. Mastrangelo, and M. Tabib-Azar, "MEMS-based hemispherical resonator gyroscopes," in *2012 IEEE SENSORS*, Oct. 2012, pp. 1–4, iSSN: 1930-0395. [Online]. Available: https://ieeexplore.ieee.org/abstract/document/6411346

[37] M. H. Asadian, D. Wang, Y. Wang, and A. M. Shkel, "3D Dual-Shell Micro-Resonators for Harsh Environments," in *IEEE/ION Position, Location and Navigation Symposium (PLANS)*. Portland, OR, USA: IEEE, Apr. 2020, pp. 1467–1471. [Online]. Available: https://ieeexplore.ieee.org/document/9109972/

[38] D. Wang, N. A. Strnad, and A. M. Shkel, "Initial Demonstration of Fused Silica Dual-Shell Gyroscope Using Indirect Method of Piezoelectric Excitation," *IEEE Sensors Letters*, vol. 7, no. 9, Sep. 2023. [Online]. Available: https://ieeexplore.ieee.org/document/10225642/

[39] J. Y. Cho, J. Yan, J. A. Gregory, H. W. Eberhart, R. L. Peterson, and K. Najafi, "3-Dimensional Blow Torch-Molding of Fused Silica Microstructures," *Journal of Microelectromechanical Systems*, vol. 22, no. 6, pp. 1276–1284, Dec. 2013, conference Name: Journal of Microelectromechanical Systems. [Online]. Available: https://ieeexplore.ieee.org/document/6589107/?arnumber=6589107

[40] J. Cho, S. Singh, T. Nagourney, J.-K. Woo, A. Darvishian, B. Shiari, G. He, C. Boyd, E. Bentley, and K. Najafi, "High-Q Navigation-Grade Fused-Silica Micro Birdbath Resonator Gyroscope," in *2021 IEEE Sensors*, Oct. 2021, pp. 1–4, iSSN: 2168-9229. [Online]. Available: https://ieeexplore.ieee.org/document/9639559

[41] J. Y. Cho, S. Singh, J.-K. Woo, G. He, and K. Najafi, "0.00016 deg/hr Angle Random Walk (ARW) and 0.0014 deg/hr Bias Instability (BI) from a 5.2M-Q and 1-cm Precision Shell Integrating (PSI) Gyroscope," in *2020 IEEE International Symposium on Inertial Sensors and Systems (INERTIAL)*, Mar. 2020, pp. 1–4. [Online]. Available: https://ieeexplore.ieee.org/document/9090086

[42] A. Darvishian, B. Shiari, J. Y. Cho, T. Nagourney, and K. Najafi, "Anchor Loss in Hemispherical Shell Resonators," *Journal of Microelectromechanical Systems*, vol. 26, no. 1, pp. 51–66, Feb. 2017, conference Name: Journal of Microelectromechanical Systems. [Online]. Available: https://ieeexplore.ieee.org/document/7807224/?arnumber=7807224

[43] J. Rodriguez, S. A. Chandorkar, C. A. Watson, G. M. Glaze, C. H. Ahn, E. J. Ng, Y. Yang, and T. W. Kenny, "Direct Detection of Akhiezer Damping in a Silicon MEMS Resonator," *Scientific Reports*, vol. 9, no. 1, p. 2244, Feb. 2019, publisher: Nature Publishing Group. [Online]. Available: https://www.nature.com/articles/s41598-019-38847-6

[44] B. S. Lunin, "Physical and Chemical Bases for Development of Hemispherical Resonators for Solid-State Gyroscopes," 2005.

[45] "COMSOL Multiphysics® v. 6.2," Stockholm, Sweden. [Online]. Available: www.comsol.com

[46] Y. Wang and A. M. Shkel, "Study on surface roughness improvement of Fused Quartz after thermal and chemical post-processing," in *2016 IEEE International Symposium on Inertial Sensors and Systems*, Feb. 2016, pp. 101–104. [Online]. Available: https://ieeexplore.ieee.org/document/7435555

[47] P. G. Steeneken, J. J. M. Ruigrok, S. Kang, J. T. M. v. Beek, J. Bontemps, and J. J. Koning, "Parameter Extraction and Support-Loss in MEMS Resonators," Apr. 2013, arXiv:1304.7953 [cond-mat]. [Online]. Available: http://arxiv.org/abs/1304.7953

[48] J. M. L. Miller, G. D. Vukasin, Z. Zhang, H.-K. Kwon, A. Majumdar, T. W. Kenny, and S. W. Shaw, "Effects of Remote Boundary Conditions on Clamping Loss in Micromechanical Resonators," *Journal of Microelectromechanical Systems*, vol. 31, no. 2, pp. 204–216, Apr. 2022, conference Name: Journal of Microelectromechanical Systems. [Online]. Available: https://ieeexplore.ieee.org/document/9674749

[49] A. Efimovskaya, D. Wang, Y.-W. Lin, and A. M. Shkel, "On ordering of fundamental wineglass modes in toroidal ring gyroscope," in *2016 IEEE SENSORS*, Oct. 2016, pp. 1–3. [Online]. Available: https://ieeexplore.ieee.org/document/7808401

[50] X. Zhou, D. Xiao, Q. Li, Q. Hu, Z. Hou, K. He, Z. Chen, C. Zhao, Y. Wu, X. Wu, and A. Seshia, "Investigation on the Quality Factor Limit of the (111) Silicon Based Disk Resonator," *Micromachines*, vol. 9, no. 1, p. 25, Jan. 2018, number: 1 Publisher: Multidisciplinary Digital Publishing Institute. [Online]. Available: https://www.mdpi.com/2072-666X/9/1/25

[51] DARPA-BAA-10-39, "Microscale Rate Integrating Gyroscope (MRIG)," Apr. 2010.

[52] D. Senkal and A. Shkel, *Whole-Angle MEMS Gyroscopes: Challenges and Opportunities*. Wiley-IEEE Press, 2019. [Online]. Available: https://ieeexplore.ieee.org/book/9107330

[53] C. Acar and A. Shkel, *MEMS Vibratory Gyroscopes: Structural Approaches to Improve Robustness*, ser. MEMS Reference Shelf. Boston, MA: Springer US, 2009. [Online]. Available: https://link.springer.com/10.1007/978-0-387-09536-3

[54] Y. Wang, M. H. Asadian, and A. M. Shkel, "Compensation of frequency split by directional lapping in fused quartz micro wineglass resonators," *Journal of Micromechanics and Microengineering*, vol. 28, no. 9, p. 095001, May 2018, publisher: IOP Publishing. [Online]. Available: https://dx.doi.org/10.1088/1361-6439/aac221

[55] B. Li, X. Xi, K. Lu, Y. Shi, D. Xiao, and X. Wu, "Frequency Split Improvement of Fused Silica Micro Shell Resonator Based on Suppression of Geometric Harmonic Error," in *2020 IEEE International Symposium on Inertial Sensors and Systems (INERTIAL)*, Mar. 2020, pp. 1–3. [Online]. Available: https://ieeexplore.ieee.org/document/9090011

[56] L. Granados, R. Morena, N. Takamure, T. Suga, S. Huang, D. R. McKenzie, and A. Ho-Baillie, "Silicate glass-to-glass hermetic bonding for encapsulation of next-generation optoelectronics: A review," *Materials Today*, vol. 47, pp. 131–155, Jul. 2021. [Online]. Available: https://www.sciencedirect.com/science/article/pii/S1369702121000456

[57] D. Vatanparvar and A. M. Shkel, "Digital Manufacturing of Resonance Mems From A Single-Layer Fused Silica Material," in *IEEE International Conference on Micro Electro Mechanical Systems Conference (MEMS)*, Jan. 2022, pp. 180–183, iSSN: 2160-1968. [Online]. Available: https://ieeexplore.ieee.org/abstract/document/9699685

Appendix A

List of Vendors

Allied High Tech Products, Inc.

Location: Cerritos, CA 90703

Phone: 310-635-2466

Email: info@alliedhightech.com

Allied High Tech Products, Inc. provides the die-level grinding and polishing instruments for release of Fused Silica shell resonators and all lapping related products, such as lapping films, slurry, lubricants, and lapping fixtures. Maintenance and repair of the Multiprep Polishing System are also available from this vendor.

Front Range Photomask Co. LLC

Location: Las Vegas, NV 89120

Phone: 702-381-2000

Email: masks@frontrange-photomask.com

Front Range Photomask Co. LLC provides glass photomask fabrication service with accuracy ranging from 0.2μm to 10μm.

Kurt J. Lesker

Location: Jefferson Hills, PA 15025, USA

Phone: 800-245-1656 Website: https://www.lesker.com/

Kurt J. Lesker is a very popular online retailer that provides a wide range of equipment used in the lab, including sputtering targets, pressure gauges, vacuum chamber parts, and more.

Mark Optics, Inc.

Location: Santa Ana, CA, USA

Phone: 714-545-6684 Email: quote@markoptics.com

Mark Optics, Inc. is a custom optics provider that specializes in glass wafers. Available materials include Pyrex, Fused Quartz, Borosilicate Glass (BSG), and Ultra Low Expansion Titania Silicate Glass (ULE TSG). Wafer polishing service for etched Dual-Shell wafers was also performed by Mark Optics, Inc.

Marvell Nanofabrication Laboratory

Location: Berkeley, CA, USA

Phone: 510-809-8600

Email (Tariq): haniff@berkeley.edu

University cleanroom providing micro-fabrication services. Specifically, double-side 2µm doped Poly-Si LPCVD is necessary as the hard mask during HF wet etching of the Fused Silica wafers. The thickness of the wafers can be as high as 2mm, they a have a custom boat to accomodate these that belongs to us. Tariq is usually in charge of this depositions and is the person to talk to. Attempts at undoped Poly-Si have been unsuccesful as a good hard-mask.

Leica Microsystems Inc.

Location: Deerfield, IL 60015

Phone: 800-248-0223

Website: https://www.leica-microsystems.com/

Manufacturer of the optical microscope used for taking measurements of asymmetries. Spare parts (replacement lamp) and microscope objective repair and purchase are available from the vendor.

PTB Sales

Location: Azusa, CA 91702

Phone: 866-332-0500

Website: https://ptbsales.com/

Local company that can perform diagnostics and repairs of Pfeiffer vacuum pumps, as well as vacuum chamber conditioning.

MTI Corp.

Location: Richmond, CA 94804-3809

Phone: 510-525-3070

Website: http://www.mtixtl.com/

Manufacturer of the custom glassblowing furnace, supplier of parts for the furnace.

UCI Machine Shop

Location: Engineering Tower, Room 444

Email (Tyler Schuldt): tschuldt@uci.edu

Machine shop in UCI. They can perform small machining jobs. They have custom tooling to be able to drill holes into the parallel polishing fixtures purchased from Allied, which are now standard for multi-sample lapping release of Dual-Shell resonators.